Actomyosin-II facilitates long-range retrograde transport of large cargoes by controlling axonal radial contractility

Tong Wang[1,3,*], Wei Li[1], Sally Martin[1,2], Andreas Papadopulos[1], Golnoosh Shamsollahi[1], Vanessa Lanoue[1], Pranesh Padmanabhan[1], He Huang[1], Xiaojun Yu[1], Victor Anggono[1,3] and Frederic A. Meunier[1,3,*]

Affiliations:

[1]Clem Jones Centre for Ageing Dementia Research, Queensland Brain Institute, The University of Queensland, Brisbane, QLD 4072, Australia.

[2]Current address: The Australian Institute for Bioengineering and Nanotechnology, The University of Queensland, Brisbane, QLD 4072, Australia.

[3]Senior author.

*Correspondence to: Tong Wang (t.wang4@uq.edu.au), or Frederic A. Meunier (f.meunier@uq.edu.au), Clem Jones Centre for Ageing Dementia Research, Queensland Brain Institute, The University of Queensland, Brisbane, Queensland 4072, Australia.

Abstract

Most mammalian neurons have a narrow axon, which constrains the passage of large cargoes such as autophagosome as they can be larger than the axon diameter. Variations in tension must therefore occur radially to facilitate changes in axonal diameter and ensure efficient axoplasmic trafficking. Here, we reveal that the transit of diverse large membrane-bound cargoes causes an acute, albeit transient, radial expansion of the axonal diameter, which is immediately restored by constricting forces. We demonstrate that non-muscle myosin II (NM-II) forms ~200 nm periodic structures, which associate with axonal F-actin rings. Inhibition of NM-II activity with blebbistatin significantly increases axon diameter without affecting the periodicity of either the F-actin rings or NM-II. This sustained radial expansion significantly affects the trafficking speed, directionality, and reduces the overall efficiency of long-range retrograde axonal cargoes, eventually leading to focal axon swelling and cargo accumulation, which are hallmarks of axonal degeneration.

Introduction

Neurons are polarized cells that contain many nerve terminal boutons separated from the cell body by a long and thin axon. Within the axon, an active bidirectional cargo transport system mediates the trafficking of proteins, lipids, membrane-bound vesicles and organelles (cargoes) that undergo retrograde or anterograde transport. Tightly regulated axonal transport is pivotal for neuronal development, communication and survival[1, 2]. Despite the heavy trafficking, quantitative electron microscopy studies have found that thin axons (inner diameter < 1 μm) are the most abundant type in the mammalian central nervous system (CNS)[3, 4]. For instance, the long-range connective axons found in the human corpus callosum have an average diameter that ranges

between 0.64 μm and 0.74 μm[3]. In contrast, the size of axonal cargoes is highly variable, encompassing autophagosomes (0.5-1.5 μm)[5], mitochondria (0.75-3 μm)[6] and endosomes (50 nm-1 μm)[7]. Thus, the range of cargo sizes is comparable to, or surprisingly even larger than some of the CNS axons themselves. This advocates for the existence of radial contractility in the axons, which would allow the transient expansion of axon calibre and facilitate the passage of large cargoes. Indeed, the expansion of axonal diameter surrounding large cargoes, *i.e.* autophagosomes[8] or mitochondria[9], has been observed by super-resolution microscopy and 2D-electron microscopy (EM) in both normal and degenerating axons[10, 11]. Considering the spatial limitation exerted by the rigid axon membrane[12], the trafficking of large cargoes is likely to be affected. In fact, a simulation study based on axon structure and intra-axonal microfluidic dynamics predicted that cargo trafficking was impeded by the friction from the axonal walls in small-calibre axons[13]. In line with this prediction, a correlation between axon diameter and axon trafficking was recently reported in *Drosophila*[14, 15] and rodent neurons[16, 17]. However, direct evidence showing whether and how axonal radial contractility affects cargo trafficking is still lacking.

We hypothesized that the underlying structural basis for axonal radial contractility is the subcortical actomyosin network, which is organized into specialized structures called membrane-associated periodic cytoskeletal structures (MPS), as revealed with super-resolution microscopy along the shafts of mature axons[18]. F-actin, together with adducin and spectrin, forms a subcortical lattice with a ~190 nm periodic interval covering the majority of the axon length[18, 19]. The disrupting of axonal F-actin leads to loss of MPS[20, 21], whereas the depletion of adducin causes progressive dilation of the axon diameter and axon loss, with slightly impaired axonal trafficking[16]. The fact that

adducin knock-out axons are still capable of decreasing the diameter of actin rings over time suggests the existence of additional actin regulatory machineries that maintain this constriction. Indeed, the dynamic contractility of the subcortical actomyosin network depends on non-muscle myosin-II (NM-II)[22], which generates the subcellular forces required to restore the shape of the cell following acute stretching[23]. In line with this function, the activated regulatory light chain (pMLC) of NM-II has recently been shown to exist in periodic patterns in close association with the MPS in the axon initiation segment (AIS) of mammalian CNS neurons[24], with actomyosin-dependent contractility being implicated in maintaining axon diameter by coupling the radial and axial axonal contractility in *Drosophila*[14]. Understanding how the dynamic cytoskeletal architecture coordinates the radial axonal contractility and cargo trafficking is therefore warranted.

In this study, we used super-resolution live-imaging approaches to examine the correlation between the speed of axonal cargoes undergoing long-range transport and their size. We found that the speed inversely correlates with the cargo size, and that the axon undergoes dynamic local deformation during the passage of large cargoes, which induces transient enlargement immediately followed by constriction of the axon diameter. We further demonstrated, using super-resolution structured illumination microscopy (SR-SIM) as well as simulated emission depletion (STED) microscopy, that this transient change in axon diameter is mediated by NM-II, which forms an approximately 200 nm periodical structure perpendicular to the longitudinal axis of axons. Our results suggest that CNS axons are under constitutive radial constriction, which limits their diameter. Accordingly, short-term inhibition of axonal NM-II activity with blebbistatin, a specific membrane-permeable inhibitor that

stabilizes myosin-II in an actin-detached state[25], does not affect the periodicity of either F-actin or NM-II itself, but rather effectively decreases their colocalization and expands the diameter of the axon. As a result of augmented axon diameter, short-term blebbistatin incubation affects the transport speed of large cargoes by increasing both the speed of fast-moving cargoes and the back-and-forth movements of stalled ones. This leads to an increase in cargo mobility at the expense of overall trafficking efficacy. Prolonged NM-II inactivation by either blebbistatin treatment or transfection of a myosin-II regulatory light chain (MRLC) loss-of-function mutant eventually leads to the formation of focal axon swellings (FAS) and the accumulation of retrograde cargoes along the axons. In conclusion, our study reveals the critical role of axonal NM-II which, by associating with subcortical MPS in the axon shaft, provides subcellular radial constriction that minimizes the axonal swelling and undirected cargo movements. It therefore ensures the structural stability as well as the cargo-trafficking efficiency along the small-calibre axons.

Results

The speed of retrograde axonal cargoes is inversely correlated with their size.

Large axonal cargoes such as endosomes, lysosomes, autophagosomes and mitochondria tend to accumulate in FAS under pathological conditions[26], suggesting that the size of cargoes might alter the axonal trafficking efficacy. To determine the relationship between the size of cargoes and their transport speed, we analyzed the speeds of various-sized retrograde lysosomal and endosomal vesicles. These cargoes were generated and fluorescent-labelled with the lysosomal marker Lysotracker or the endosomal marker Cholera toxin subunit B (CTB) at the nerve terminals, and underwent retrograde trafficking along the axon bundles of live hippocampal neurons

cultured in microfluidic devices (Fig. 1a, b). Hydrostatic pressure was used to restrict the labelling reagents to the terminal chamber during the 5 min pulse-labelling (Fig. 1c). This was followed by a thorough wash in culture medium to remove the excess fluorescent probe and confocal time-lapse imaging and automatic tracing of the fluorescently tagged cargoes as previously described[8, 27, 28]. To investigate different stages of axonal trafficking, live-imaging was performed in two distinct axonal regions: (1) the axon shafts adjacent to the soma chamber (Fig. 1d, left) and (2) within the terminal chamber (Fig. 1d, right). Lysotracker-labelled vesicles detected in the nerve terminal chamber exhibited very confined movements (sFig. 1a and sMov. 1). We further quantified the average speed of these tracks, which were sorted into two different groups according to their diameter (sFig. 1a, bottom panels). We observed that vesicles with a large diameter ('large', diameter > 0.5 μm) moved significantly slower (0.115 ± 0.039 μm/s) than those with a smaller diameter ('small', diameter ≤ 0.5 μm; 0.159 ± 0.006 μm/s), as shown in sFig. 1b. This suggests that transport of large axonal cargoes in axons surrounding nerve terminals could be impeded during their transit. To specifically investigate the correlation between the size of axonal cargoes and their active transport speed, we further examined the trafficking speed of long-range CTB-positive retrograde carriers in the soma-proximal axon channels (Fig. 1e-g). Consistent with our previous study[29], these long-range carriers exhibited a much faster trafficking speed (0.974-1.659 μm/s) than the carriers at nerve terminals (0.115-0.159 μm/s; Fig. 1g; sFig. 1b). Similar to the lysosomes in the nerve terminals, the trafficking speed of these CTB-positive carriers also inversely correlated with their diameter, with small-diameter cargoes moving faster (1.657 ± 0.06 μm/s) than large-diameter ones (0.974 ± 0.05 μm/s; Fig. 1g; sMov. 2). We then examined the

correlation between cargo size and speed by plotting the apparent diameter of either lysosomal carriers or CTB-positive carriers against their speed. This revealed a negative correlation, with a Pearson's coefficient of -0.303 ± 0.095 and -0.273 ± 0.036 between cargo diameter and trafficking speed in the terminal ("Lysotracker", Fig. 1h) and proximal ("CTB", Fig. 1h) axons, respectively, indicating that the speed of the trafficked cargoes declines as the cargo size increases.

Transit of large cargoes causes a significant radial expansion of the axon.

Each organelle undergoing retrograde axonal transport is driven by multiple dyneins, which are stochastically activated and collectively drive cargo transport through the axonal cytosol[30-32]. Given the low viscosity of axonal cytosol, the force generated by cooperative dyneins is sufficient to ensure their retrograde trafficking through the axon[32]. Thus, the reduced speed of the larger cargoes we observed is unlikely due to insufficient driving force or a higher viscous load due to the larger size. Considering the recent evidence suggesting the role of axon diameter in axon cargo trafficking[14-16], we hypothesized that the size-dependent friction on the axonal cargoes comes from the constrictive force exerted by the axonal plasma membrane, which is more likely to impede the transport of larger retrograde cargoes.

To test this hypothesis, we examined the diameter of axons in the presence or absence of cargoes at the ultrastructural level. In order to eliminate confounding factors related to the analysis of dendrites, experiments were only performed on axonal bundles formed within the channels of microfluidic devices[8, 27, 28], as shown in Fig. 2a. We first used EM to visualize the morphology of both axon shafts and their internal cargoes. As demonstrated in Fig. 2b-c, on the parallel axonal bundles, the diameters of axons were indeed significantly increased around large cargoes, such as large

166 endosomes (Fig. 2c, i, arrow), mitochondria (Fig. 2c, ii and iii, white arrowheads) and
167 autophagosomes (Fig. 2c, iii and iv, black arrowheads). When we measured the
168 diameter of the axonal segment with (red) and without cargo (blue) in the same axon,
169 we found that those with cargoes had a significantly larger diameter (347 ± 15.6 nm)
170 than those without cargoes (259 ± 9.4 nm; Fig. 2d) with paired comparison. We also
171 observed that, as the size of the cargoes increased, the extent of axon expansion also
172 increased proportionally (Fig. 2e, f), suggesting that the stretch of the axon membrane
173 is indeed caused by the transiting cargo.
174
175 We next investigated the effect of transiting cargoes on the diameter of axons in live
176 hippocampal neurons. To effectively label the subcortical actomyosin network in
177 axons, we used Lifeact-GFP, a peptide that binds to both actin filaments (F-actin) and
178 cytosolic actin monomers[33]. Similar to a previous study[34], with the resolution of SIM,
179 we detected Lifeact-GFP distribution in both the filamentous and cytosolic fractions
180 in axons of live hippocampal neurons (Fig. 3a), with the plasma membrane labelled
181 by CTB-Alexa555. Interestingly, the improved 3D-SIM resolution allowed us to
182 observe various-sized intra-axonal fluorescence voids ("black-holes") that likely
183 represent axoplasmic organelles (Fig. 3b), which are known to exclude actin from
184 their lumens[35]. Similar to the cargo-induced axon dilation observed with EM, the axon
185 diameter was also significantly expanded in axon segments with black-holes (Fig. 3c).
186 We then characterized the nature of these black-holes by comparing their localization
187 with that of various organelle markers resolved by 3D-SIM, and found substantial
188 overlap with autophagosomes (LC3-mRFP, Fig. 3d), late endosomes (Rab7-mRFP,
189 Fig. 3e) and mitochondria (Mito-TagRFP, Fig. 3f). This suggests that these black-
190 holes were indeed created by large organelles, which caused significant local dilation

of the axon (Fig. 3g). To further investigate whether these black-holes were cargoes that associate with the transport machinery, we determined their colocalization with markers of retrograde carriers, such as terminal-derived CTB[27] and the neuron-specific dynein intermediate chain 1B (DIC^{1B})[36]. The black-holes partially overlapped with CTB- and DIC^{1B}-positive axonal structures (Fig. 3h, i), indicating that a substantial portion of them were indeed caused by retrograde trafficking organelles in live axons.

Next, we investigated whether the transit of cargoes correlated with the local axon dilation in live axons. Using time-lapse SIM and unbiased Gaussian fitting (Fig. 4a), we assessed the fluctuations in axon diameter and clearly detected radial diameter expansion through the transient separation of the two lateral axonal membranes, which caused an increase in the distance between the centre of the Gaussians (Fig. 4b; sMov. 3). This effect was transient and the initial diameter was restored after the passage of the organelles (black-holes), as shown in Fig. 4c. In addition, the association between diameter expansion and the passage of lysotracker- and CTB-positive carriers was also observed by phase-contrast confocal microscopy (Fig. 4d-e). Taken together, our results demonstrate that radial dilation of the axon diameter is caused by the passage of cargoes in the axons of live hippocampal neurons.

NM-II forms periodic structures that associate with F-actin MPS and controls the radial contractility of axon.

The contractility and plasma membrane tension of cells is controlled by NM-II. To investigate whether NM-II is involved in the cargo-associated radial dilation of axons, we treated Lifeact-GFP-expressing neurons with blebbistatin, and examined the

cargo-associated diameter fluctuations of their axons. We observed that blebbistatin treatment (10 μM, 60 min) caused a significant relaxation of the axon shaft by increasing axon diameter with (ϕ_{+cargo}) and without (ϕ_{-cargo}) cargoes (Fig. 5a, b). We then explored the diameter fluctuations by comparing the average ratio of axon diameter containing cargoes to that without cargoes, and used this ratio ($\phi_{+cargo}/\phi_{-cargo}$) as an index of the cargo-associated diameter fluctuations. Blebbistatin treatment significantly decreased this index, resulting in more uniformly dilated axons (Fig. 5c). These results suggest that radial contractility of the axon shaft is dependent on the NM-II activity of the actomyosin network.

To further explore the molecular basis of the axonal radial contractility, we sought to resolve the actomyosin structure along the axon shafts. As F-actin and its associated proteins are known to form MPS in axons[18, 19, 21], we first aimed to characterize the actin MPS along the axon shaft using SIM, which had previously been used to accurately visualize axon MPS[37]. In cultured hippocampal neurons, phalloidin staining of F-actin allowed the observation of MPS formed along the axon shaft with a conserved longitudinal spacing of ~190 nm (Fig. 5d; sFig. 2a), as quantified using the frequency distribution of spacing between adjacent actin peaks detected using phalloidin-647 (191.8 ± 2.3 nm; Fig. 5e-f; sFig. 2b) or Lifeact-GFP (sFig. 2c-g), and confirmed by auto-correlation analysis (184.6 ± 4.1 nm; Fig. 5g). Obtained values were similar to those previously reported in rat hippocampal axons[18, 21]. As NM-II is involved in the regulation of axonal diameter[14] and associated with the MPS in axons[24], we also examined whether blocking NM-II activity affected the spacing of actin MPS. 60 min of blebbistatin treatment had no effect on this spacing (Fig. 5e, f). However, this short-term treatment significantly increased the radial diameters of the

241 actin rings in treated axons (Fig. 5d, h), causing a more uniformly dilated actin MPS,
242 as reflected by the decreased ring diameter fluctuation (Fig. 5i). These results are
243 consistent with the effect of blebbistatin on axonal diameter expansion in live axons.
244 The significant dilation of actin MPS caused by detaching NM-II suggests that the
245 interaction between NM-II and actin MPS underlies the radial contractility of axons.
246
247 To examine this hypothesis and assess the relationship between the distribution of
248 endogenous NM-II and actin MPS along the axon shaft, we used dual-colour 3D-SIM .
249 We co-labeled the axons of DIV14 rat hippocampal neuron with phalloidin and an
250 antibody that recognizes the C-terminus central domain of NM-IIB (αNM-II(ct)), the
251 dominant form of NM-II in axons[24], and we observed that NM-II exhibited a periodic
252 distribution (Fig. 6a, b), with an average spacing of 197.5 ± 3.1 nm (Fig. 6c, d), which
253 is similar to the periodicity determined by the autocorrelation method (187.4 ±9.8 nm,
254 Fig. 6e). To further examine the orientation and periodicity of the NM-II filaments
255 along the axon, we used another NM-IIB antibody that recognizes its N-terminal head
256 domain (αNM-II(nt)) and which was previously used to detect a bipolar structure of
257 NM-II filaments with super-resolution microscopy[38, 39]. Using super-resolution
258 stimulated emission depletion (STED) microscopy (sFig. 3a), we found that the
259 αNM-IIB(nt) stained for a bipolar structure that had a periodic spacing of 206.4 ± 2.6
260 nm along the axons (sFig. 3c). These values were consistent with that of
261 phosphorylated-MLC spacing, as reported recently[24]. Interestingly, these bipolar NM-
262 II structures presented a perpendicular orientation to the axon axis in both mono-
263 colored αNM-IIB(nt) stained axons detected by 3D-STED (sFig. 3b) and the dual-
264 colored αNM-IIB(nt) and αNM-IIB(ct) co-stained axons detected by 3D-SIM (sFig.
265 3d, e).

We also examined the correlation between the actin and NM-II MPS distribution, and noted that they exhibited both overlapping (arrows, Fig. 6b; sFig. 4a, b) and alternating (arrowheads, Fig. 6b; sFig. 4a, b) distribution patterns, which were reflected by the high cross-correlation coefficient of 0.684 ± 0.091 (Fig. 6f, at 0 nm shift). However, we failed to detect an obvious cross-periodicity between actin and NM-II (Fig. 6f), which was probably due to the fact that the periodicity between these two patterns is beyond the resolution limit of SIM (~100 nm). We next investigated whether the localization pattern of NM-II was affected by the inhibition of its activity, and found that short-term blebbistatin treatment did not significantly change the NM-II spacing (Fig. 6c-e), but significantly decreased the degree of cross-correlation between NM-II and actin MPS (0. 414 ± 0.073 (0 nm); Fig. 6f). Indeed, it was apparent that NM-II and actin MPS distributed more discretely from each other in the axons of blebbistatin-treated neurons (Fig. 6a, b, bottom panels). This reduction in NM-II and actin correlation was further supported by the reduced colocalization between NM-II and actin voxels following blebbistatin treatment, as resolved from the 3D-SIM images (sFig. 4b-d).

To confirm that the NM-II indeed correlated with actin MPS in the subcortical network, which is associated with the axonal plasma membrane, we adopted the method of Triton X-100 extraction before fixation to specifically remove the subcortical actin MPS components as previously reported[20]. Following this extraction, we observed a significant reduction in actin MPS (sFig. 4e, f), confirming the disruption of the membrane-associated actin MPS. Together with this reduction, we detected a dramatic reduction in NM-II positive puncta (sFig. 4e, g). This concomitant

decrease in both actin MPS and NM-II (sFig. 4h) further supports the notion that NM-II correlates with actin MPS in the membrane-associated subcortical network. Together, these results indicate that NM-II controls the contraction of the subcortical actin MPS, which underlies the radial contractility of axons.

Short-term inhibition of NM-II activity causes sustained axon dilation and interferes with the long-range retrograde trafficking of large cargoes.

To test whether axon radial contractility has a functional role in cargo transport, we examined the effect of blebbistatin on retrograde axonal trafficking in neurons grown in a 6-well microfluidic device (sFig. 5a), where we could restrict the action of blebbistatin to the axon segments by adding it through the middle chamber (sFig. 5b). Widespread dilation of the axons diameter along their longitudinal direction was observed following 90 min of blebbistatin incubation (sFig. 5c-e). To test the integrity of these treated axons, we further examined the axonal microtubule structure by dual-color SIM using a β-tubulin III antibody and phalloidin (sFig. 5f). We found that neither the microtubule bundle intensity (sFig. 5g) nor width (sFig. 5h) were affected by 60 min blebbistatin treatment. This blebbistatin treatment also failed to affect the mitochondrial anchoring, as the movement of the immobile mitochondrial fraction was not affected (sFig. 5i, j), whereas the mobile fractions with the higher average speeds were significantly increased by the blebbistatin movement (sFig. 5i, j), suggesting that the NM-II-dependent axonal contractility is likely to affect the cargo transport.

To further assess the effects of axonal contractility on cargo trafficking, we examined the impact of disrupting NM-II activity on retrograde trafficking in short-term

316 blebbistatin-treated axons. The average speed of CTB-positive carriers before (pre)
317 and after (+BLB) blebbistatin treatment for 60 min (Fig. 7a) were compared. As
318 demonstrated earlier (Fig. 1g), small carriers moved faster than large ones in the
319 absence of blebbistatin (Fig. 7b), whereas blebbistatin treatment specifically increased
320 the trafficking speed of large CTB-positive carriers, but not that of small ones (Fig. 7b
321 and sMov. 4). Similarly, an increase of the average speed was observed for large
322 Lysotracker-positive carriers, but not for small ones (Fig. 7c, sMov. 5). These results
323 indicate that the short-term relaxation of the axonal actomyosin-II network has an
324 initial positive impact on the trafficking of large cargoes, suggesting that axon radial
325 contractility exerts a local brake on their transport.
326
327 Given that the large CTB-positive carrier population showed the most significant
328 increase in speed upon blebbistatin treatment (Fig. 7b), we chose this type of carriers
329 for more detailed motion analyses, in order to further dissect the impact of radial
330 contractility on axonal transport. By tracking the transport of individual CTB-carriers
331 within the microfluidic channels (Fig. 7a), we noted that their trajectories were
332 predominately composed of two mobility states: (i) a fast-moving state and (ii) a
333 stalled state, as indicated by the sloped and the vertical lines, respectively, in the
334 displacement-time plot (Fig. 7d). Following 60 min blebbistatin treatment, the speed
335 of the fast-moving state was significantly increased, as indicated by the flatter slopes
336 (Fig. 7d), whereas in the stalled state we observed pronounced back-and-forth motion
337 (Fig. 7d, asterisks and sMov. 4), which has been previously described as low-
338 efficiency trafficking pattern for long-range cargo transport[40]. We noticed an increase
339 in the ratio of the fast-moving CTB-carriers (sFig. 5k) and a decrease in that of the
340 slow-moving ones (sFig. 5k). To further quantify these back-and-forth movements,

we compared the ratio of direction swap (*Sr*) in these tracks by measuring the ratio of the time cargoes spent travelling in the reverse direction (t_{rev}) in relation to the total time travelled (t_{total}), as shown in equate (1), with k being the number of trajectories.

$$Sr = \frac{\sum_{k=0}^{n} {t_{rev}}^k}{\sum_{k=0}^{n} {t_{total}}^k} \quad (1)$$

This analysis revealed that blebbistatin treatment significantly increased the amount of time cargoes underwent reverse motion, thereby increasing the ratio of direction swap in cargoes moving along the axon (Fig. 7e). Accordingly, we found that blebbistatin treatment decreased the number of CTB-positive carriers that traversed the imaging window within a given time (Fig. 7f), suggesting that the overall retrograde trafficking efficiency was reduced. These results support the positive role of axonal radial contractility in maintaining near-unidirectional retrograde trafficking, thereby ensuring the overall efficiency of long-range retrograde transport.

We next investigated how the radial contractility impacted the mobility of the fast-moving and stalled carriers, respectively, by analyzing the dynamics of the CTB-positive carrier movements. To objectively and quantitatively analyze the effect of the contractility on the two motion states, we employed a two-state hidden Markov model (HMM) to annotate these CTB trajectories into stalled (D) and transport (DV) states (Fig. 7g), as previously described[28]. The separating efficacy of this model was demonstrated by the fact that the step size of the stalled (0.1168 ± 0.45 μm) and transport states (0.4352 ± 1.53 μm) were distinct from each other. We then examined the effect of blebbistatin treatment, and found that it significantly increased the step size of large CTB-positive carriers in the DV state (Fig. 7h, pink spots), which is in good agreement with our earlier observations (Fig. 7b and sMov. 4). For the D state in

365 pretreated axons, CTB-positive carriers exhibited a much smaller step size (Fig. 7h),
366 meaning that the mobility of these stalled carriers was constrained. However, this
367 limited step size was significantly increased following 60 min blebbistatin treatment
368 (Fig. 7h, blue spots). Consistent with the increased back-and-forth movements (Fig.
369 7d, e), this result suggests that the mobility of the stalled carriers is increased
370 following disruption of NM-II activity. Taken together, our findings indicate that the
371 axonal actomyosin network maintains radial constriction, which not only impedes the
372 speed of the fast-moving state but also suppresses the low-efficiency back-and-forth
373 movement during the stall state of these long-range carriers. The overall impact of this
374 contractility on long-range trafficking is therefore positive, which facilitates the uni-
375 directionality and the overall efficiency of long-range retrograde carriers.
376
377 ***Prolonged inactivation of actomyosin-II causes focal axon swelling accompanied***
378 ***with stalled cargo accumulation.***
379 In addition to 60 min blebbistatin treatment, we also examined the impact of longer
380 exposure to blebbistatin on both axon structure and trafficking. We discovered that
381 prolonged blebbistatin treatment (60 - 120 min) increased the percentage of axons
382 with focal swellings (Fig. 8a, b), which was represented by the gradual formation of
383 FAS (Fig. 8a), with these FAS becoming prevalent (59.85 ± 5.159 %) following long-
384 term blebbistatin treatment (10 μM, 120 min, Fig. 8b). As FAS is a hallmark of
385 irreversible axonal damage[11], these results suggested that disrupting radial
386 contractility could directly lead to FAS and ensuing axonal degeneration.
387
388 To fully assess the effects of radial axon contractility on retrograde cargo trafficking,
389 we further resolved the impact of long-term NM-II inhibition on the long-range

trafficking of retrograde endosomal CTB-positive carriers (Fig. 8c). We found that both the trafficking speed (Fig. 8d) and transverse frequency (Fig. 8e) of these carriers were significantly reduced after 120 min blebbistatin treatment. To assess whether the axonal radial contractility affects trafficking efficiency of other retrograde cargoes, we also compared the trafficking efficacy of autophagosome (LC3-mRFP labelled), which undergoes long-range retrograde trafficking[8, 41], in axons in the presence or absence of blebbistatin (120 min treatment). We found that similar to CTB-positive carriers, the trafficking speed of these LC3-mRFP-positive carriers was also significantly reduced (Fig. 8f, g). Importantly, we also observed the gradual accumulation of the stalled LC3-carriers at FAS (Fig. 8f, h). In addition to pharmacological inactivation of NM-II, we also transfected the myosin-II regulatory light chain with the S19AT18A mutations, ($MRLC^{mut}$-GFP), which abolishes the ability of NM-II to bind to and slide along the F-actin[42]. We found that 48 hours after $MRLC^{mut}$-GFP transfection, the structural integrity of transfected axons was significantly disrupted as reflected by the significantly increased diameter fluctuations (Fig. 8i, j) and FAS formation (Fig. 8k) compared to those transfected with wild-type controls ($MRLC^{wt}$-GFP). These results suggest that the long-term inactivation of actomyosin-II not only impairs axonal trafficking but also causes irreversible structural damage to the axon, which may eventually lead to its degeneration.

Discussion

Many factors affect long-range axonal cargo trafficking, including the number and type of attached molecular motors[43, 44], the polarity of the microtubule tracks[45], and friction from other organelles[46]. With the development of live-imaging microscopy, most of these factors have been extensively studied in cell-free *in vitro* systems[44], and within the axons of cultured neurons[32, 47] and live animals[48]. However, the impact of the narrow and rigid axonal plasma membrane on the transiting cargoes remains largely elusive. In this study, we have demonstrated that the transport of large membrane-bound cargoes causes an acute, albeit transient, radial stretching of the axonal plasma membrane, which is immediately restored by constitutive constricting forces generated by the membrane-associated periodic actomyosin-II network. We have also identified NM-II as a critical regulator of this radial contractility, which controls not only the speed but also the directionality of long-range cargo trafficking along the axon. Inactivation of this contractility machinery eventually leads to stalled cargo trafficking and FAS, which are early signs of axon degeneration. Our study therefore reveals novel functions of the actomyosin-II network in facilitating the efficacy of long-range axonal trafficking and maintaining the structural stability of CNS axons.

Radial contractility facilitates the overall efficiency of long-range retrograde axonal trafficking.

An efficient long-range retrograde cargo transport machinery is critical for the survival and function of neurons[1, 2, 48]. Retrograde trafficking is thrusted by cytoplasmic dynein[49], which drives the near-unidirectional retrograde transport of

nerve terminal-derived signalling endosomes and autophagosomes to the cell body[8, 32]. Detailed analysis of the movement of these carriers has revealed that they are mainly composed of fast-moving retrograde-directed and stalled carriers, with less than 3% being reverse-directed (anterograde) carriers[8, 27]. A similar near uni-directional motion pattern is shared by retrograde endosomes carrying nerve growth factor (NGF)[32] and tetanus toxins[50]. The retrograde directionality of the fast-moving cargoes is driven by the progressive minus-end-directed dynein steps, the directionality of which is dependent on the opposing forces they received[49]. Actomyosin controls radial contractility, which poses a steric hindrance to the passaging cargoes[46] and therefore could potentially affects the opposing force to their driven dyneins. However, the effect of the axonal actomyosin network on the dynein-driven trafficking is poorly understood. Early studies provided evidence that disrupting F-actin in axons does not interfere with organelle transport, which continues unabated or at an even faster rate[51], suggesting that the axonal F-actin network acts as a physical impediment to cargo transport. In line with this, we found that short-term blebbistatin treatment released subcellular tension, causing an expansion of the axon diameter and specifically increasing the transport speed of large cargoes. Our results therefore confirm that the fast-moving state of large cargoes is subjected to a constant impediment from radial axonal constriction. On the other hand, the stalling of retrograde carriers is likely to be caused by either a balanced tug-of-war between kinesin and dynein[52], or the transient detachment of dynein-driven carriers from the microtubule tracks[40, 49]. Our data using HMM-Bayesian partition show an increased mobility of stalled carriers after blebbistatin treatment, which suggests that axonal radial constriction might affect the microtubule attachment/tethering of these stalled carriers within the axon. This could be due to the tension-dependent tethering of dynein to the microtubule tracks[53].

459 However, further study on the coordination between cargo trafficking and local axon
460 radial tension, using higher temporal resolution live-imaging techniques, is needed to
461 establish the precise relationship between axonal radial constriction and the motion of
462 various-sized retrograde carriers.
463
464 ***The actomyosin-II network is the structural basis for the contractility of axon shafts.***
465 The diameter of the long and thin axon has long been believed to be uniform for the
466 same type of neurons. However, with the development of 3D EM reconstruction,
467 diameter fluctuations have been detected along the length of axons in optical nerves[10].
468 Similarly, in live rat brains, axonal diameter fluctuations were revealed with super-
469 resolution microscopy after the conduction of action potentials[54]. Consistent with
470 these *in vivo* studies, we have used EM, SR-SIM and bright-field confocal microscopy
471 to reveal that axons undergo dynamic diameter fluctuations. With time-lapse SR-SIM
472 and confocal microscopy, we further correlated the dynamic radial expansion of the
473 axonal diameter with the passage of large cargoes. These deformations are highly
474 correlated with the transit of various types of large cargoes and are therefore most
475 likely caused by this. These transient deformations also suggest the existence of a
476 mechanical tension derived from the axonal plasma membrane. Atomic force
477 microscopy studies have identified the axon as the most rigid neuronal segment,
478 which is under constitutive tension[12] from the ordered periodic longitudinal
479 MPS composed of actin, spectrin, adducin and associated proteins[18]. Disruption of
480 actin and spectrin abolished the actin MPS, whereas adducin depletion did not affect
481 its spacing but still caused dilation and degeneration of axons[16]. However, the radial
482 contractility of adducin knockout axons remained unaltered, suggesting the existence
483 of an alternative mechanism for the contractility along the axon shafts.

In mammalian cells, radial contractility of subcortical actin[55] or actin rings[35] is regulated by mechanosensory NM-II, which is the major cytoskeletal complex in neurons with the ability to convert ATP into mechanical force. Recently, the activated form of NM-II light chain (pMLC) was shown to distribute in a similar periodicity and largely overlap with the actin MPS at the AIS[24]. Moreover, depolarization rapidly decreased NM-II activity, further suggesting that this constricting structure is highly dynamic[24, 56]. Consistent with these previous studies, we reveal a periodic pattern of NM-II of ~200 nm by dual labelling with phalloidin-647 and an NM-IIB C-terminus antibody. In addition, cross-correlation analysis of these two MPS demonstrates a substantial colocalization, which is significantly reduced by blebbistatin-induced NM-II detachment. Further, our results demonstrate that NM-II periodicity goes far beyond the AIS, and confirm the existence of periodic actomyosin rings, which provide the structural basis for axonal radial contractility. Higher resolution three-colour microscopic techniques are needed to further resolve the precise conformational changes that occur at the level of the actomyosin-II MPS as large cargoes pass through.

Over-expansion of axonal segments, such as FAS, has been noted in several neurodegenerative diseases, with the accumulation of organelles and cargoes at the axonal swellings - the presence of FAS is generally regarded as an early sign of axonal degeneration[11]. Similar to FAS, diameter dilation, cargo accumulation and degeneration were also observed in axons of adducin knock out mice[16], as well as in axons following prolonged blebbistatin treatment (>120 min) or transfection with the inactive MRLC mutant in this study, suggesting that the actomyosin-II-dependent

509 radial contractility is critical to maintain the structural stability of the axon. Additional
510 studies will be required to directly characterize the contractility changes in FAS and
511 to examine whether enhancing radial contractility could have any rescuing effect.
512
513 In summary, we have uncovered an inverse correlation between axonal cargo size and
514 trafficking speed, and demonstrated that axons undergo transient deformation caused
515 by the cargo transition in hippocampal axon bundles. We have further identified the
516 periodic structure of actomyosin-II along the axon shaft as the structural basis of
517 axonal radial contractility. We have also characterized its role in facilitating long-
518 range cargo trafficking by restricting inefficient back-and-forth cargo movement
519 during the stall state. Our data identify a novel role for the axonal actomyosin-II
520 network in long-range cargo trafficking, and highlight the importance of axonal
521 membrane tension in ensuring the efficiency of this trafficking.
522

Online Methods

Antibodies, molecular reagents and DNA constructs

Alexa-555- and Alexa-647-conjugated recombinant CTB were obtained from ThermoFisher Scientific (#c-34776, #c-34777). Mouse anti-synaptobrevin-2 (VAMP2) antibody was obtained from Synaptic Systems (#104 211) and the rabbit anti-NM-IIB(ct) polyclonal antibodies were from Sigma-Aldrich (#M7939), mouse anti-NM-IIB(nt) monoclonal from Santa Cruz (sc-376954). Alexa-647-phalloidin was purchased from Invitrogen (#A22287), while the mouse anti- β-tubulin III was from Covance (#MMS-435P). Alexa Fluor secondary antibodies were purchased from Life Technologies. The DNA construct encoding Lifeact-GFP was provided by Roland Wedlich Soldner (MPI Biochemistry, Martinsried), pTagRFP-mito was purchased from Evrogen (#FP147), pmRFP-LC3 was a gift from Tamotsu Yoshimori (Addgene plasmid # 21075). Lysotracker Deep Red came from ThermoFisher (#L12492). The remaining reagents were obtained from Electron Microscopy Sciences or Sigma Aldrich unless otherwise specified.

Neuronal cultures

Hippocampal neurons were cultured from embryonic day 18 (E18) embryos from Sprague Dawley rats. All experiments were approved by The University of Queensland Animal Ethics Committee. Hippocampal neurons were prepared as described previously[8] and were plated on either glass coverslips (for confocal microscopy), plastic dishes (for EM) or in microfluidic chambers (Xona, #RD450) according to the manufacturer's protocol[57]. For the pretreated groups, live-imaging of approximate 5 (30×12 μm) regions of interest (ROIs) was performed 2 h after the CTB labelling. For blebbistatin treatment, conditioned culture medium containing

548 blebbistatin (10 μM) was only added to the middle and/or terminal chambers of the 6-
549 well or 4-well microfluidic chambers (Xona, #TCND500; #RD450) to exclude its
550 effect on the soma. For the short-term blebbistatin treatment, microfluidic devices
551 were immediately returned to the 37^{o}C imaging chamber for live imaging, and
552 approximately 5 ROIs were imaged within a total duration of 60 min. For long-term
553 blebbistatin treatment, microfluidic devices were returned to a 37^{o}C CO_2 incubator for
554 an additional 2h before continuing the live imaging.
555
556 ***Confocal microscopy***
557 Stimulation and labelling were carried out on rat hippocampal neurons cultured in
558 microfluidic chambers between day *in vitro* 14 (DIV14). Briefly, the culture medium
559 was removed from all chambers and the neurons were incubated for 5 min at 37˚C in
560 labelling buffer (15 mM HEPES, 95 mM NaCl, 56 mM KCl, 2.2mM $CaCl_2$, 0.5mM
561 $MgCl_2$, 5.6mM D-glucose, 0.5 mM ascorbic acid, 0.1% bovine serum albumin (BSA),
562 pH 7.4), with 50 ng/ml CTB-Af555 or CTB-Af647 added to the nerve terminal
563 chambers only. For Lysotracker labelling, the incubation time was 30 min. Neurons
564 were then washed 3 times with warm neurobasal medium and returned to the original
565 conditioned growth medium for 2 h prior to imaging. Images were acquired with a
566 Zeiss LSM710 inverted microscope maintained at 37˚C and 5% CO_2, and movies
567 were analysed for carrier kinetics using the spot function of Imaris software
568 (Imaris7.7-9.2, Bitplane). Kymographs were generated using ImageJ software (NIH)
569 using the plugin Multi-Kymograph for ImageJ. For immunofluorescence microscopy
570 of fixed cells, the microfluidic devices were removed and neurons were subsequently
571 fixed for 2-4 h at 4^{o}C with phosphate buffered saline (PBS) containing 4%
572 paraformaldehyde and 4% sucrose, followed by immunostaining as previously

described[27]. Permeabilization was performed using 0.1% saponin, 0.2% gelatin, and 1% BSA in PBS. Imaging was carried out on a Zeiss LSM710 confocal microscope and analysed with Zen (Zeiss) and ImageJ softwares. All images were compiled using Illustrator CS 5.1 (Adobe).

Imaris tracing of axonal cargoes

Time-lapse movies of CTB-positive or Lysotracker-positive carriers were analysed for carrier kinetics using the spot function of Imaris software (Imaris7.7-9.2, Bitplane). In brief, region growth was enable (threshold 50, diameter from border mode), estimated diameter 0.75 μm, tracing with autogressive motion (Max Distance 2 μm, Max Gap size 0). Resulted trajectories were filtered with duration > 10 s and instant speed > 0.07 μm/s. Average speed are calculated as track length divided by track duration. For Lysotracker-positive carriers that bleaches rapidly, only the diameter of the first time point in each trajectory were used as the diameter for size grouping.

Co-labelling of F-actin and NM-II for SR-SIM

Cultured rat hippocampal neurons were fixed at DIV14. For dual-colour imaging of actin and NM-IIB, the fixation protocol was modified from that previously established for maintaining actin ultrastructure[18]. Briefly, the samples were initially fixed in 4% paraformaldehyde dissolved in cytoskeleton buffer (CB, 10 mM MES, 150 mM NaCl, 5 mM EGTA, 5 mM glucose and 5 mM $MgCl_2$, pH 6.1) for 30 min at room temperature and then blocked with antibody dilution buffer (2% BSA with 0.1% Triton X-100 in PBS) for 1 h at room temperature, after which the primary antibody (NM-IIB, diluted 1 in 500) and phalloidin-Af647 (0.14 μM) in 2% BSA in PBS were applied to the dish and incubated at 4^{o}C overnight. Donkey anti-rabbit secondary

antibody (Thermofisher, #A-21206) was diluted at 1/500 and incubated for 1h at room temperature. Samples were immediately mounted in Vectashield medium (Vector Laboratories, #H-1000) for SIM imaging. For the Triton X-100 extraction experiment, neurons were first treated with the extraction buffer (4% paraformaldehyde, 0.1% (v/v) Triton X-100, 1 µg/ml phalloidin in CB) for 45 s before the fixation and staining steps.

Structured illumination microscopy

Imaging of live or fixed samples was performed using an ELYRA PS1 SR-SIM system (Zeiss) equipped with a 100x objective (α Plan-Apochromat 100×/1.46 oil-immersion DIC M27) and a CMOS camera (PCO Scientific). For live-imaging of the Af555-CTB- labelled neurons, images were obtained with the Fastframe mode (100 ms exposure time, a time serie of 200 frames at 1.44 s intervals, a SIM grating size of 42 µm at 561 nm wavelengths, and using 3 rotations). For fixed and stained samples, images were obtained by acquiring z-stacks of 10-16 slices with a spacing of 0.101 µm, an exposure time of 100 ms, a SIM grating size of 42-51 µm, and using five rotations. 3D structured illumination images were then aligned and processed using the Zen software. For cross-correlation analysis, line profiles were selected based on the standard of the existence of at least 4 consecutive NM-II peaks in a single axon shafts. The intensity profiles of each of the channels were then obtained using the Multichannel plot profile function of BAR collection (DOI10.5281/zenodo.28838) in ImageJ software (NIH). The auto-correlation or cross-correlation rate between the different channels was then examined using the xcorr function of Matlab. The correlation values for each axon segment were averaged and plotted.

Simulated emission depletion (STED) microscopy

Cultured rat hippocampal neurons (DIV14-17) cultured in glass bottom dishes were imaged on a Leica SP8 confocal with STED 3X. (DMI8 stand with 775nm, 660nm 592nm STED lasers and a white-light tuneable laser for excitation). Images were acquired using the HC plan apochromat 100x 1.4 NA oil immersion objective using Leica LASX software with 3 frame accumulations as multi-slice z-stacks. Deconvolution was performed using up to 40 cycles of iterative deconvolution using Huygens Professional. Images were visualised and maximum intensity projected using FIJI (NIH).

Assessment of actin MPS and NM-II abundance

Periodic cytoskeletal structures (MPS) are defined as the axonal regions with at least 4 consecutive actin or NM-II peaks along the longitudinal direction. 5-7 of 5 μm × 5 μm ROIs were selected along the axons in each 3D-SIM image (50 μm × 50 μm). In each ROI, the length of axon with F-actin MPS was measured with ImageJ by a trained observer blind to the treatment conditions. In the same ROI, the particle number of NM-II staining was also automatically quantified with the Analyse Particle plugin of FIJI. MPS or NM-II abundance were then calculated as the percentage of segments length with an MPS or particle number over the total length of axons in the ROI respectively.

Electron microscopy

Rat hippocampal neurons cultured in microfluidic devices (14-17 DIV) were treated as described for confocal microscopy[27], except that 10 μg/ml CTB-HRP was added to the nerve terminal chambers for the period of stimulation. Cells were returned to growth medium for 4 h prior to fixation. All cells were fixed in 2.5% glutaraldehyde

for 24 h. Following fixation, they were processed for 3, 39-diaminobenzidine (DAB) cytochemistry using the standard protocol. Fixed cells were contrasted with 1% osmium tetroxide and 4% uranyl acetate prior to dehydration and embedding in LX-112 resin[58]. Sections (~50 nm) were cut using an ultramicrotome (UC64; Leica). To quantify CTB-HRP endocytosis, presynaptic regions were visualized at 60,000x using a transmission electron microscope (model 1011; JEOL) equipped with a Morada cooled CCD camera and the iTEM AnalySIS software. Membrane-bound compartments within the cell soma proximal region of the microfluidic channel were analysed, and the axon diameter measured using ImageJ software.

HMM-Bayes analysis

Hidden Markov model (HMM) method was used to predict the particle hidden states and the state transition probabilities from experimental trajectories. By using Bayesian model selection in the inference process, the simplest mobility model can be selected to describe these trajectories in an objective manner[59]. We analysed the trajectories from each cell of interest using HMM-Bayes software[60]. A maximum of 2 hidden states was set to describe the trajectory movements, diffusion motion (D) and active transport state (DV), which were used to describe the stalled state and the fast-moving state, respectively. In our cases, at least 10 channel ROIs were quantified for the control group and the blebbistatin-treated group, with corresponding trajectory numbers being 126 and 190 respectively. The D state with a low apparent diffusion coefficient state representing the immobile unattached movement. The DV state, which could be described by averaged velocity, represents the active transport attached movement. All of the analyses were performed using Matlab (R2016a,

672 MathWorks, Inc.). The average step sizes of different transport states was calculated
673 from all D-DV models.
674
675 ***Statistics***
676 We used GraphPad Prism 7 (GraphPad Inc.) for statistical analyses. Results are
677 reported as mean ± s.e.m. For group comparisons, two-tailed nonparametric *t*-tests
678 or paired *t*-tests were executed. *P* values < 0.05 indicated statistical significance.
679 No statistical methods were used to predetermine sample sizes. Data distribution was
680 assumed to be normal, but this was not formally tested. There was no formal
681 randomization. Data collection and analysis were performed by different operators,
682 who were blind to the conditions of the experiments.
683

References

1. Tojima, T. & Kamiguchi, H. Exocytic and endocytic membrane trafficking in axon development. *Dev Growth Differ* **57**, 291-304 (2015).
2. Barford, K., Deppmann, C. & Winckler, B. The neurotrophin receptor signaling endosome: Where trafficking meets signaling. *Dev Neurobiol* **77**, 405-418 (2017).
3. Liewald, D., Miller, R., Logothetis, N., Wagner, H.J. & Schuz, A. Distribution of axon diameters in cortical white matter: An electron-microscopic study on three human brains and a macaque. *Biol Cybern* **108**, 541-57 (2014).
4. Perge, J.A., Niven, J.E., Mugnaini, E., Balasubramanian, V. & Sterling, P. Why do axons differ in caliber? *J Neurosci* **32**, 626-38 (2012).
5. Mizushima, N., Ohsumi, Y. & Yoshimori, T. Autophagosome formation in mammalian cells. *Cell Struct Funct* **27**, 421-9 (2002).
6. McBride, H.M., Neuspiel, M. & Wasiak, S. Mitochondria: More than just a powerhouse. *Curr Biol* **16**, R551-60 (2006).
7. Altick, A.L., Baryshnikova, L.M., Vu, T.Q. & von Bartheld, C.S. Quantitative analysis of multivesicular bodies (mvbs) in the hypoglossal nerve: Evidence that neurotrophic factors do not use mvbs for retrograde axonal transport. *J Comp Neurol* **514**, 641-57 (2009).
8. Wang, T., *et al.* Control of autophagosome axonal retrograde flux by presynaptic activity unveiled using botulinum neurotoxin type-a. *Journal of Neurochemistry* **134**, 165 (2015).
9. Yin, X., *et al.* Proteolipid protein-deficient myelin promotes axonal mitochondrial dysfunction via altered metabolic coupling. *J Cell Biol* **215**, 531-542 (2016).

709 10. Giacci, M.K., *et al.* Three dimensional electron microscopy reveals changing
710 axonal and myelin morphology along normal and partially injured optic
711 nerves. *Sci Rep* **8**, 3979 (2018).
712 11. Maia, P.D., *et al.* Diagnostic tools for evaluating the impact of focal axonal
713 swellings arising in neurodegenerative diseases and/or traumatic brain injury.
714 *J Neurosci Methods* **253**, 233-43 (2015).
715 12. Zhang, Y., *et al.* Modeling of the axon membrane skeleton structure and
716 implications for its mechanical properties. *PLoS Comput Biol* **13**, e1005407
717 (2017).
718 13. Wortman, J.C., *et al.* Axonal transport: How high microtubule density can
719 compensate for boundary effects in small-caliber axons. *Biophys J* **106**, 813-
720 23 (2014).
721 14. Fan, A., Tofangchi, A., Kandel, M., Popescu, G. & Saif, T. Coupled
722 circumferential and axial tension driven by actin and myosin influences in
723 vivo axon diameter. *Sci Rep* **7**, 14188 (2017).
724 15. Narayanareddy, B.R., Vartiainen, S., Hariri, N., O'Dowd, D.K. & Gross, S.P.
725 A biophysical analysis of mitochondrial movement: Differences between
726 transport in neuronal cell bodies versus processes. *Traffic* **15**, 762-71 (2014).
727 16. Leite, S.C., *et al.* The actin-binding protein alpha-adducin is required for
728 maintaining axon diameter. *Cell Rep* **15**, 490-498 (2016).
729 17. Pesaresi, M., *et al.* Axon diameter and axonal transport: In vivo and in vitro
730 effects of androgens. *Neuroimage* **115**, 191-201 (2015).
731 18. Xu, K., Zhong, G. & Zhuang, X. Actin, spectrin, and associated proteins form
732 a periodic cytoskeletal structure in axons. *Science* **339**, 452-6 (2013).

19. Han, B., Zhou, R., Xia, C. & Zhuang, X. Structural organization of the actin-spectrin-based membrane skeleton in dendrites and soma of neurons. *Proc Natl Acad Sci U S A* **114**, E6678-E6685 (2017).

20. Zhong, G., *et al.* Developmental mechanism of the periodic membrane skeleton in axons. *Elife* **3** (2014).

21. He, J., *et al.* Prevalent presence of periodic actin-spectrin-based membrane skeleton in a broad range of neuronal cell types and animal species. *Proc Natl Acad Sci U S A* **113**, 6029-34 (2016).

22. Arnold, D.B. & Gallo, G. Structure meets function: Actin filaments and myosin motors in the axon. *J Neurochem* **129**, 213-220 (2014).

23. Papadopulos, A., *et al.* Activity-driven relaxation of the cortical actomyosin ii network synchronizes munc18-1-dependent neurosecretory vesicle docking. *Nat Commun* **6**, 6297 (2015).

24. Berger, S.L., *et al.* Localized myosin ii activity regulates assembly and plasticity of the axon initial segment. *Neuron* **97**, 555-570 e6 (2018).

25. Kovacs, M., Toth, J., Hetenyi, C., Malnasi-Csizmadia, A. & Sellers, J.R. Mechanism of blebbistatin inhibition of myosin ii. *J Biol Chem* **279**, 35557-63 (2004).

26. Tammineni, P., Ye, X., Feng, T., Aikal, D. & Cai, Q. Impaired retrograde transport of axonal autophagosomes contributes to autophagic stress in alzheimer's disease neurons. *Elife* **6** (2017).

27. Wang, T., *et al.* Flux of signalling endosomes undergoing axonal retrograde transport is encoded by presynaptic activity and trkb. *Nat Commun* **7**, 12976 (2016).

28. Joensuu, M., *et al.* Visualizing endocytic recycling and trafficking in live neurons by subdiffractional tracking of internalized molecules. *Nat Protoc* **12**, 2590-2622 (2017).

29. Joensuu, M., *et al.* Subdiffractional tracking of internalized molecules reveals heterogeneous motion states of synaptic vesicles. *J Cell Biol* **215**, 277-292 (2016).

30. Rai, A.K., Rai, A., Ramaiya, A.J., Jha, R. & Mallik, R. Molecular adaptations allow dynein to generate large collective forces inside cells. *Cell* **152**, 172-82 (2013).

31. Mallik, R., Petrov, D., Lex, S.A., King, S.J. & Gross, S.P. Building complexity: An in vitro study of cytoplasmic dynein with in vivo implications. *Curr Biol* **15**, 2075-85 (2005).

32. Chowdary, P.D., Che, D.L., Zhang, K. & Cui, B. Retrograde ngf axonal transport--motor coordination in the unidirectional motility regime. *Biophys J* **108**, 2691-703 (2015).

33. Riedl, J., *et al.* Lifeact: A versatile marker to visualize f-actin. *Nat Methods* **5**, 605-7 (2008).

34. Ganguly, A., *et al.* A dynamic formin-dependent deep f-actin network in axons. *J Cell Biol* **210**, 401-17 (2015).

35. Gormal, R.S., Nguyen, T.H., Martin, S., Papadopulos, A. & Meunier, F.A. An acto-myosin ii constricting ring initiates the fission of activity-dependent bulk endosomes in neurosecretory cells. *J Neurosci* **35**, 1380-9 (2015).

36. Ha, J., *et al.* A neuron-specific cytoplasmic dynein isoform preferentially transports trkb signaling endosomes. *J Cell Biol* **181**, 1027-39 (2008).

781 37. Qu, Y., Hahn, I., Webb, S.E., Pearce, S.P. & Prokop, A. Periodic actin
782 structures in neuronal axons are required to maintain microtubules. *Mol Biol*
783 *Cell* **28**, 296-308 (2017).
784 38. Hu, S., *et al.* Long-range self-organization of cytoskeletal myosin ii filament
785 stacks. *Nat Cell Biol* **19**, 133-141 (2017).
786 39. Beach, J.R., *et al.* Nonmuscle myosin ii isoforms coassemble in living cells.
787 *Curr Biol* **24**, 1160-6 (2014).
788 40. Yi, J.Y., *et al.* High-resolution imaging reveals indirect coordination of
789 opposite motors and a role for lis1 in high-load axonal transport. *J Cell Biol*
790 **195**, 193-201 (2011).
791 41. Maday, S., Wallace, K.E. & Holzbaur, E.L. Autophagosomes initiate distally
792 and mature during transport toward the cell soma in primary neurons. *J Cell*
793 *Biol* **196**, 407-17 (2012).
794 42. Beach, J.R., Licate, L.S., Crish, J.F. & Egelhoff, T.T. Analysis of the role of
795 ser1/ser2/thr9 phosphorylation on myosin ii assembly and function in live
796 cells. *BMC Cell Biol* **12**, 52 (2011).
797 43. Hancock, W.O. Bidirectional cargo transport: Moving beyond tug of war. *Nat*
798 *Rev Mol Cell Biol* **15**, 615-28 (2014).
799 44. Vale, R.D., Malik, F. & Brown, D. Directional instability of microtubule
800 transport in the presence of kinesin and dynein, two opposite polarity motor
801 proteins. *J Cell Biol* **119**, 1589-96 (1992).
802 45. Kapitein, L.C. & Hoogenraad, C.C. Which way to go? Cytoskeletal
803 organization and polarized transport in neurons. *Mol Cell Neurosci* **46**, 9-20
804 (2011).

805 46. Che, D.L., Chowdary, P.D. & Cui, B. A close look at axonal transport: Cargos
806 slow down when crossing stationary organelles. *Neurosci Lett* **610**, 110-6
807 (2016).
808 47. Chowdary, P.D., *et al.* Nanoparticle-assisted optical tethering of endosomes
809 reveals the cooperative function of dyneins in retrograde axonal transport. *Sci*
810 *Rep* **5**, 18059 (2015).
811 48. Bilsland, L.G., *et al.* Deficits in axonal transport precede als symptoms in
812 vivo. *Proc Natl Acad Sci U S A* **107**, 20523-8 (2010).
813 49. Gennerich, A., Carter, A.P., Reck-Peterson, S.L. & Vale, R.D. Force-induced
814 bidirectional stepping of cytoplasmic dynein. *Cell* **131**, 952-65 (2007).
815 50. Lalli, G., Bohnert, S., Deinhardt, K., Verastegui, C. & Schiavo, G. The
816 journey of tetanus and botulinum neurotoxins in neurons. *Trends Microbiol*
817 **11**, 431-7 (2003).
818 51. Morris, R.L. & Hollenbeck, P.J. Axonal transport of mitochondria along
819 microtubules and f-actin in living vertebrate neurons. *J Cell Biol* **131**, 1315-26
820 (1995).
821 52. Belyy, V., *et al.* The mammalian dynein-dynactin complex is a strong
822 opponent to kinesin in a tug-of-war competition. *Nat Cell Biol* **18**, 1018-24
823 (2016).
824 53. Cleary, F.B., *et al.* Tension on the linker gates the atp-dependent release of
825 dynein from microtubules. *Nat Commun* **5**, 4587 (2014).
826 54. Chereau, R., Saraceno, G.E., Angibaud, J., Cattaert, D. & Nagerl, U.V.
827 Superresolution imaging reveals activity-dependent plasticity of axon
828 morphology linked to changes in action potential conduction velocity. *Proc*
829 *Natl Acad Sci U S A* **114**, 1401-1406 (2017).

830 55. Duan, R., *et al.* Spectrin is a mechanoresponsive protein shaping fusogenic
831 synapse architecture during myoblast fusion. *Nat Cell Biol* **20**, 688-698
832 (2018).
833 56. Evans, M.D., Tufo, C., Dumitrescu, A.S. & Grubb, M.S. Myosin ii activity is
834 required for structural plasticity at the axon initial segment. *Eur J Neurosci* **46**,
835 1751-1757 (2017).
836 57. Taylor, A.M., *et al.* A microfluidic culture platform for cns axonal injury,
837 regeneration and transport. *Nat Methods* **2**, 599-605 (2005).
838 58. Harper, C.B., *et al.* Dynamin inhibition blocks botulinum neurotoxin type a
839 endocytosis in neurons and delays botulism. *J Biol Chem* **286**, 35966-76
840 (2011).
841 59. Persson, F., Linden, M., Unoson, C. & Elf, J. Extracting intracellular diffusive
842 states and transition rates from single-molecule tracking data. *Nat Methods* **10**,
843 265-9 (2013).
844 60. Monnier, N., *et al.* Inferring transient particle transport dynamics in live cells.
845 *Nat Methods* **12**, 838-40 (2015).
846

Acknowledgements

This work was supported by grants from the Australian Research Council (ARC, DP170102402 to VA; ARC DE170100546 to TW) and the Australian National Health and Medical Research Council (NHMRC; GNT1138452 to VA and GNT1120381 to FAM). FAM is an NHMRC Senior Research Fellow (GNT1060075). TW is an ARC DECRA Fellow (DE170100546) and was previously supported by a The University of Queensland Postdoctoral Research Fellowship. HH and XJY were recipients of University of Queensland Research Training Scholarships. Imaging was performed at the Queensland Brain Institute's Advanced Microscopy Facility, generously supported by the Australian Government through the ARC LIEF Grant (LE130100078 to FAM). Electron microscopy was performed at the Australian Microscopy and Microanalysis Facility, The University of Queensland. The authors would like to thank Rowan Tweedale for editing the manuscript, and Joanne Jang, Rumelo Amor, Nicholas Condon, Luke Hammond, Nick Valmas and Rachel Gormal for expert technical assistance.

Author contributions

FAM and TW designed the study, supervised the project and wrote the manuscript. TW performed live-imaging microscopy, confocal and SIM experiments and analysed data. WL performed HMM separation and assisted with data analysis. SM designed and performed EM experiments and helped with data analysis. AP designed and performed the analysis of particle speed and swap, and helped with SIM. GS helped to develop the staining protocol for dual-colour SIM. XJY and HH helped with primary neuronal culture, transfection, analysis of LC3-mRFP data. VA supervised works conducted by XJY, HH and WL, and edited the manuscript. VL and PP helped with

872 the edition of the manuscript and the figures. All authors discussed the results and
873 commented on the manuscript.
874
875 **Competing Interests**
876 The authors declare no competing interest.
877
878 **Materials & correspondence**
879 Correspondence and requests for materials should be addressed to Prof. Frederic A.
880 Meunier (f.meunier@uq.edu.au) and Dr Tong Wang (t.wang4@uq.edu.au).
881
882 **Data availability**
883 All other data supporting the findings of this study are available from the
884 corresponding authors upon reasonable request.

885

886 ***Figure legends***

887 ***Figure 1. The speed of retrograde axonal transport cargoes is inversely correlated***

888 ***with their size.***

889 **(a)** Microfluidic chambers to isolate unidirectional axon bundles, bar =1 cm (adapted

890 from Xonamicrofluidics.com). (**b)** Schematic diagram of the pulse-chase labelling

891 process. Cultured hippocampal neurons were grown in a microfluidic device for 14

892 days *in vitro* (DIV). The nerve terminal chamber was incubated with fluorescently

893 tagged CTB (50 ng/ml) for 5 min or Lysotracker Deep Red (50 nM) for 30 min

894 (pulse). After thorough washes and a 2h chase. (**c)** Representative images of cultured

895 neurons, showing the restriction of retrograde CTB surface labelling to nerve

896 terminals and the position of the observation window (white box). Scale bar = 50 μm.

897 **(d)** The axonal retrograde transport of CTB or Lysotracker was monitored, at the level

898 of the proximal axon shafts or in the nerve terminal chamber, respectively. (**e)** Time-

899 lapse images of CTB carriers. Top panels: CTB labelling and tracing trajectories

900 within the axon channels. Trajectories of small (#1, diameter ≤ 0.5 μm) and large (#2,

901 diameter > 0.5 μm) carriers are magnified in the bottom panels, respectively. (**f)**

902 Representative kymographs of CTB-positive cargoes along a single axon, depicting

903 track displacements of small and large carriers. x-bar = 10 μm; y-bar = 10 s. (**g)**

904 Grouped analysis of the average speeds of CTB cargoes with small (diameter ≤ 0.5

905 μm) and large (diameter > 0.5 μm) diameters. Data represent mean ± s.e.m (small,

906 n=187, large n=185 tracks from 3 independent preparations; two-tailed unpaired t-test,

907 ***p<0.001). (**h)** Pearson's coefficient of the speed and diameter of retrograde

908 Lysotracker-positive and CTB-positive cargoes. Data represent mean ± s.e.m from 3

909 independent preparations (random, n=3 simulated data sets; Lysotracker, n=6 ; CTB,

n=14; n represents the number of axon channels analysed; the single value of the average correlation coefficient between the size and speed of all trajectories in each axon channel was calculated and used for the plot. 3 Independent groups of Gaussian-distributed random numbers were generated using the *normrnd* function of Matlab. Two-tailed unpaired t-test, **p<0.01, *p<0.05).

Figure 2. The size of axonal cargoes correlates with the diameter of the axon.

(a) Brightfield image of DIV14 rat hippocampal neurons cultured in a microfluidic device with the region selected for EM outlined. Scale bar = 250 μm. (**b)** Representative electron micrographs showing the axonal diameter measurements with cargo (red) or without cargo (blue), and the associated cargo size (white). Scale bar = 0.5 μm **(c)** Electron micrographs of axon bundles from hippocampal neurons cultured in microfluidic devices. (**i-iv)** Axon diameters with and without cargo are marked with red and blue arrows, respectively. (**i)** Endosome = black arrow, (**i-iii)** Mitochondria = white arrowheads, autophagosome = black arrowheads. (**iv)** Inner diameters of cargoes are marked with white arrows. Bars = 500 nm. (**d)** Quantification of axon diameters with cargo and without cargo. Data represent mean ± s.e.m, n= 182 (+ Cargo) and 182 (- Cargo) measurements from 2 independent preparations (two-tailed paired t-test, ***p<0.001). (**e)** Grouped quantification of axonal diameter as a function of binned vesicle size. Data represent mean ± s.e.m; for the + Cargo group from left to right: n=104, 23, 41 and 14 measurements; for the - Cargo group from left to right: n=104, 23, 41 and 22 measurements, data were from 2 independent preparations (two-tailed unpaired t-test, *p<0.05; ***p<0.001). (**f)** Cross-correlation analysis of cargo size and axonal diameter. Linear regressions were

934 performed with the 182 paired measurements of axonal and cargo diameters of the (+
935 Cargo) group, data from 2 independent preparations.
936
937 ***Figure 3. Large retrograde cargoes produce "black-holes" within the axons of***
938 ***Lifeact-GFP-expressing neurons.***
939 **(a)** Rat hippocampal neurons transfected with Lifeact-GFP were pulse-labelled with
940 CTB for 5 min and immediately subjected to 2D-SIM imaging; boxed regions of
941 axonal segments are shown on the right. Relative localization of plasma membrane
942 (CTB-labelled, arrowheads), F-actin (Lifeact-GFP; asterisk) and cytosolic actin
943 (Lifeact-GFP; arrows). Bar = 10 μm (right), 1 μm (left). (**b)** Rat hippocampal neurons
944 were transfected with Lifeact-GFP and imaged with 3D-SIM. Top: a representative
945 maximum projection of 3D-SIM of Lifeact-GFP expressing axons are shown; Bar = 5
946 μm. Bottom: magnified regions of interest (ROIs) in top panel, arrowheads indicate
947 black-holes with low Lifeact-GFP signals within the axon. Bar = 1μm. (**c)**
948 Quantification of axon diameters with (+) and without (-) black-holes. Data represent
949 mean ± s.e.m from 3 independent preparations (+ black-hole, n=29, - black-hole,
950 n=29 axons; two-tailed unpaired *t*-test, ***$p<0.001$). (**d-e)** Cultured hippocampal
951 neurons grown in a microfluidic device were transfected on DIV12 with Lifeact-GFP
952 and co-transfected with either LC3-mRFP (autophagosome) (**d)**, Rab7-mRFP (late
953 endosome) (**e)** or Mito-TagRFP (mitochondria) (**f)**, and subjected to time-lapse
954 imaging on DIV 14. Representative dual-colour 3D-SIM projections of neurons
955 expressing Lifeact-GFP and with different subcellular markers are magnified in right
956 panels, and overlapping regions are annotated. Bar = 5 μm. (**g)** Quantification of axon
957 diameters with (+) and without (-) annotated markers. Data represent mean ± s.e.m
958 (n=10 axons for each marker from 3 independent cultures; two-tailed unpaired t-test,

959 ***p*<0.01; ****p*<0.001). (**h-i)** Representative dual-colour 3D-SIM projections of
960 axons expressing Lifeact-GFP, which were co-labelled with the retrograde cargo
961 marker CTB (**h)** or DIC[1B] (**i)**. Boxed regions are magnified in right panels,
962 overlapping regions are annotated. Bar = 2 μm (**h)** and 5 μm (**i)**.
963
964 ***Figure 4. The transit of cargo causes a transient radial expansion of the axon.***
965 **(a)** Rat hippocampal neurons cultured in a glass-bottom dish were transfected with
966 Lifeact-GFP (DIV 12) and imaged by time-lapse SIM (DIV 14). Representative live
967 axons with cargo-associated black-holes passing through are shown, with inset
968 demonstrating the Gaussian fittings of the annotated line transection of axon. Bar =
969 0.5 μm (inset). (**b)** Time-lapse images of bracketed region in A, showing the axonal
970 diameter fluctuation as the cargo (indicated with red bar) transits. (**c)** Plot of the
971 distance between axon membranes against time. (**d-e)** Live-confocal imaging of axons
972 carrying CTB-positive (**c)** or Lysotracker-positive (**d)** cargoes. Magnified images of
973 the boxed region are shown in the lower panels, and moving cargoes are indicated
974 with arrowheads. Bar = 10 μm.
975
976 ***Figure 5. Short-term inactivation of NM-II increases the axon diameter without***
977 ***affecting the actin ring periodicity.***
978 **(a)** SIM images of a Lifeact-GFP-expressing axon from a DIV14 rat hippocampal
979 neuron, before and after short-term blebbistatin treatment (10 μM, 60 min). Boxed
980 regions are magnified in right panels. Axon diameter with and without cargoes is
981 indicated by arrowheads and arrows respectively. Bar = 0.4 μm. (**b)** Axon diameter
982 quantification. Data represent mean ± s.e.m, n=29, 29, 37, 37 axons from left to right.
983 Values were measured from 3 independent cultures (two-tailed unpaired t-test,

984 ***p<0.001) (**c)** Analysis of axon diameter fluctuation. Data represent mean ± s.e.m,
985 n=29 (pre), 22 (+BLB) axons from left to right. Values were measured from 3
986 independent cultures (two-tailed unpaired t-test, ***p<0.001). (**d)** SIM images of
987 endogenous F-actin (phalloidin) along the axon of a DIV14 rat hippocampal neuron
988 before and after short-term blebbistatin treatment (10 µM, 60 min). Bracketed regions
989 are magnified on the right, and the diameters of actin rings are shown below. (**e, f)**
990 Comparison of periodic actin spacing distribution (**e)** and average value (**f)** in control
991 and blebbistatin-treated neurons. Data represent mean ± s.e.m, n=300 (Control), 316
992 (+BLB) for periodicity quantification. (**g)** Autocorrelation analysis of the actin
993 periodicity of control and blebbistatin-treated axons. Data represent mean ± s.e.m, n =
994 10 (Control) and 8 (+BLB) axon segments were measured. (**h)** Distribution of actin
995 diameters in control and blebbistatin-treated axons. Data represent mean ± s.e.m, n =
996 42 (Control) and 46 (+BLB) actin rings diameters were measured. (**i)** Quantification
997 of actin ring diameter fluctuations; the diameters per 10 µm axon segments were
998 measured and quantified. Data represent mean ± s.e.m, n=11 (Control) and 11 (+BLB)
999 axon segments were analysed. Values were measured from 3 independent cultures
1000 (two-tailed unpaired t-test, n.s. no significant difference; **p<0.05; ***p<0.001).
1001
1002 ***Figure 6. NM-II immunostaining reveals a periodic pattern that correlates with the***
1003 ***periodic actin rings along the axons.***
1004 ***(*a)** Dual-colour SIM images of endogenous F-actin (phalloidin) and NM-IIB in
1005 control and blebbistatin-treated axons of DIV14 rat hippocampal neurons. Boxed
1006 regions are magnified in right panels. Bar = 1 µm (left) and 0.5 µm (right). Discrete
1007 distributions of NM-II and actin are marked with arrows in bottom panels. (**b)** A line
1008 profile was used to characterize the periodic actin ring and NM-II structures.

Overlapping and alternating peaks are marked with arrows and arrowheads respectively. (**c-e)** Comparison of NM-II distribution in control and short-term (60 min) blebbistatin-treated axons. Due to the staining efficiency of the NM-II antibody, only the spacing between at least 4 consecutive NM-II puncta were analysed. The Gaussian distribution (**c)** autocorrelation (**d)** and scattered plot (**e)** of NM-II spacing are shown. Data represent mean ± s.e.m, n = 8 (pre) and 9 (+BLB) axon segments were analysed for autocorrelation; n = 262 (Control), 261 (+BLB) NM-II puncta were analysed for periodic distribution. Data are from 3 independent cultures (two-tailed unpaired t-test, n.s. no significant difference). (**f)** Comparison of NM-II and actin ring cross-correlation in control and short-term (60 min) blebbistatin-treated axons; significant reduction of cross-correlation after blebbistatin treatment is annotated at 0 nm shifts. Data represent mean ± s.e.m; n = 5 (Control), 6 (+BLB) axon segments were analysed. Values were from 3 independent cultures (two-tailed unpaired t-test, ***$p<0.001$).

Figure 7. Short-term inactivation of actomyosin-II reduces the efficiency of retrograde axonal trafficking.

(a) DIV 14 rat hippocampal neurons were cultured in microfluidic devices, and the axon segments were subjected to short-term blebbistatin treatment (10 µM, 60 min). Trajectories of CTB-positive cargoes in the axon channels were traced before (pre) and after (+BLB) blebbistatin treatment. Bar = 10 µm. (**b, c)** Track speed (trajectory length/duration) of the CTB carriers (**b)** or Lysotracker carriers (**c)** before (pre) and after (+BLB) blebbistatin treatment. The speeds of these carriers were sub-grouped according to their diameters. Data represent mean ± s.e.m, n=187, 185, 271, 286 (CTB) and n=179, 342, 128, 573 (Lysotracker) trajectories from 3 independent

cultures (two-tailed unpaired t-test, *p<0.05, ***p<0.001, n.s. no significant difference). The same data of pre-treated groups were used in Figure 1G and Figure S1B. (**d)** Displacement-time plot of representative CTB trajectories. (i) Fast moving state, and (ii) stalled state, as magnified on the right, with the back-and-forth movements marked with asterisks. x-bar = 10 µm, y-bar= 20 s. (**e)** Time ratio of cargo travelling in the reverse direction (swap) to total time travelled. Data represent mean ± s.e.m, n=28 (Pre) and 34 (+BLB) channels from 3 independent preparations (two-tailed unpaired t-test, ***p<0.001). (**f)** Quantification of the frequency of CTB-labelled vesicles that cross the observation window per minute. Data represent mean ± s.e.m, n = 51 (Pre) and 32 (+BLB 60') channels from 3 independent preparations (two-tailed unpaired t-test, *p<0.05). (**g)** CTB trajectory displays stalled (D, blue) and fast-moving (DV, pink) motion states inferred by HMM-Bayes analysis. Example of an annotated trajectory colour-coded with the indicated motion states. The time line shows the temporal (s) sequence of the inferred D and DV motion states. (**h)** Step sizes of the two motion states before (pre) and after (+BLB) blebbistatin treatment. Data represent mean ± s.e.m, from left to right, n= 126, 126, 190, 190 different trajectories from 3 independent preparations (two-tailed unpaired t-test, ***p<0.001).

Figure 8. Long-term inhibition of actomyosin-II activity triggers accumulation of stalled cargo in focal axonal swellings (FAS).

(**a)** Hippocampal neurons (DIV 14) expressing Lifeact-GFP were incubated with blebbistatin (10 µM) for the indicated durations. Time-lapse SIM images showing morphological changes. The bracketed regions are magnified. Bar = 2 µm (left); 1 µm (right). (**b)** Percentage of axons with FAS following short-term (60 min) and long-term (120 min) blebbistatin treatment. Data represent mean ± s.e.m, n=10 (Pre), 9

(+BLB, 60 min) and 10 (+BLB, 120 min) independent ROIs were analysed. (**c-e)** Representative channel overlapping with CTB trajectories is shown in (**c**). Quantification of the track speed (**d)** and transverse frequency (**e)** of CTB carriers following long-term (120 min) blebbistatin treatment. Bar = 10 μm. Data represent mean ± s.e.m; for track speed analysis, n=185 (Pre), 286 (60 min) and 215 (120 min) trajectories, the same data sets of large cargo speed in pre-treated groups were used in Fig. 1g and Fig. 7b; for frequency analysis, n=51 (pre), 32 (60 min) and 13 (120 min) independent channel ROIs were analysed. (**f)** DIV 14 hippocampal neurons expressing Lifeact-GFP and LC3-mRFP were incubated with blebbistatin (10 μM, 120 min), with the accumulated autophagosome cargoes marked by asterisks. Kymograph of an axon is shown in the bottom panel. x-bar = 10 μm, y-bar = 60 s. (**g)** Quantification of the average speed of LC3 cargoes, and the number of FAS accompanied with LC3 cargo accumulation (**h)**, following long-term blebbistatin treatment. Data represent mean ± s.e.m; for LC3 speed, n= 72 (Pre), n=68 (120 min) trajectories; for the FAS percentage, n=10 (Pre), 9 (120 min) independent ROIs. All data were from 3 independent cultures (two-tailed unpaired t-test, *p<0.05; ***p<0.001). **(i)** Rat hippocampal neurons were co-transfected on DIV12 with the Lifeact-mRFP and either myosin-II regulatory light chain wild-type or S19AT18A mutant (MRLC^{mut}-GFP) plasmids. On DIV14 the diameter fluctuations **(j)** and FAS numbers per μm **(k)** of transfected axons were quantified. Data represent mean ± s.e.m; for actin ring fluctuation **(j)**, n= 25 (wt), n=45 (mut) independent axonal segments are measured; for the FAS counts **(k)**, n=9 (wt), 26 (mut) independent axons are counted. Data were from 2 independent preparations (two-tailed unpaired t-test, ***p<0.001).

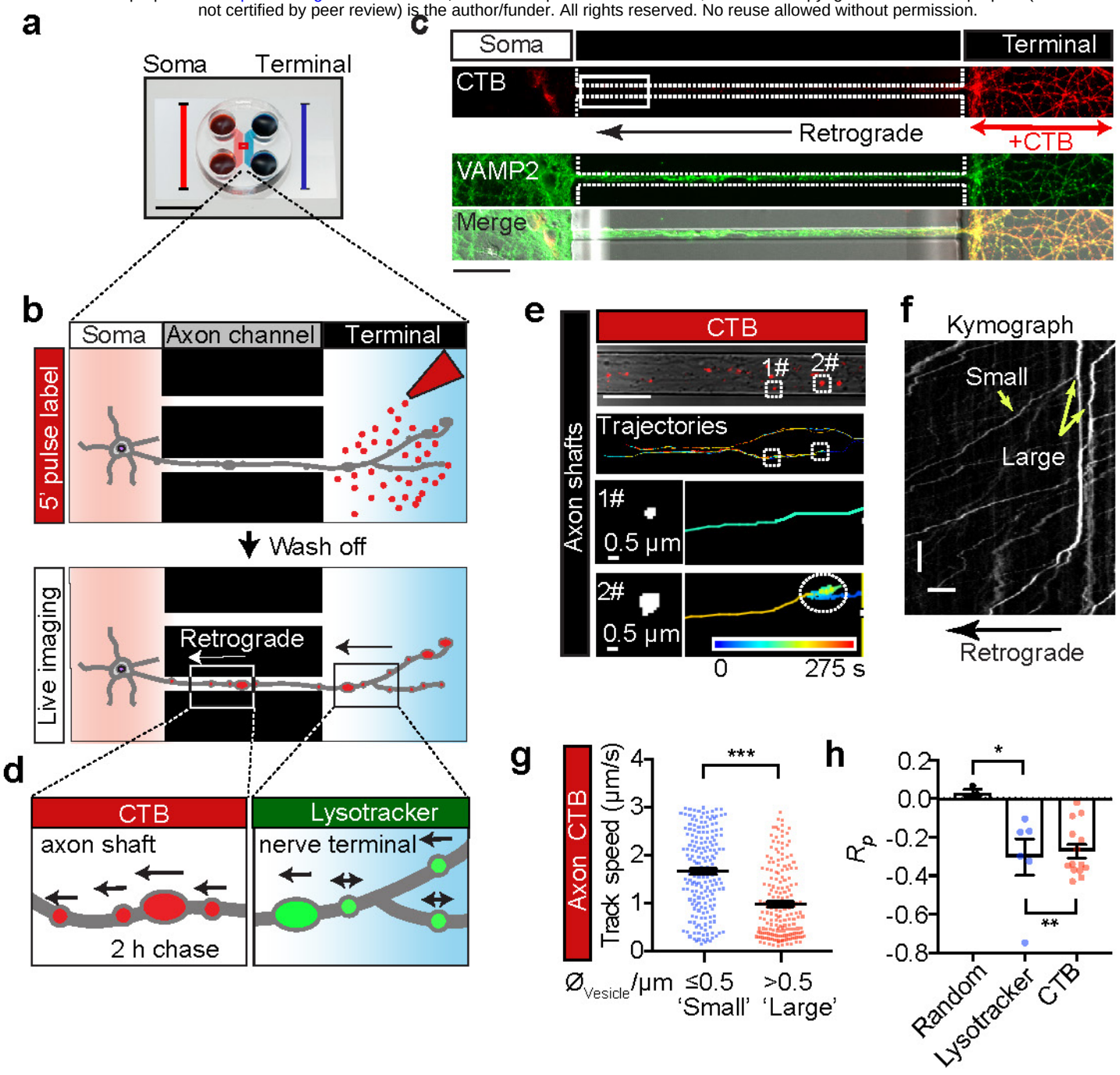

Figure 1. The speed of retrograde axonal transport cargoes is inversely correlated with their size.

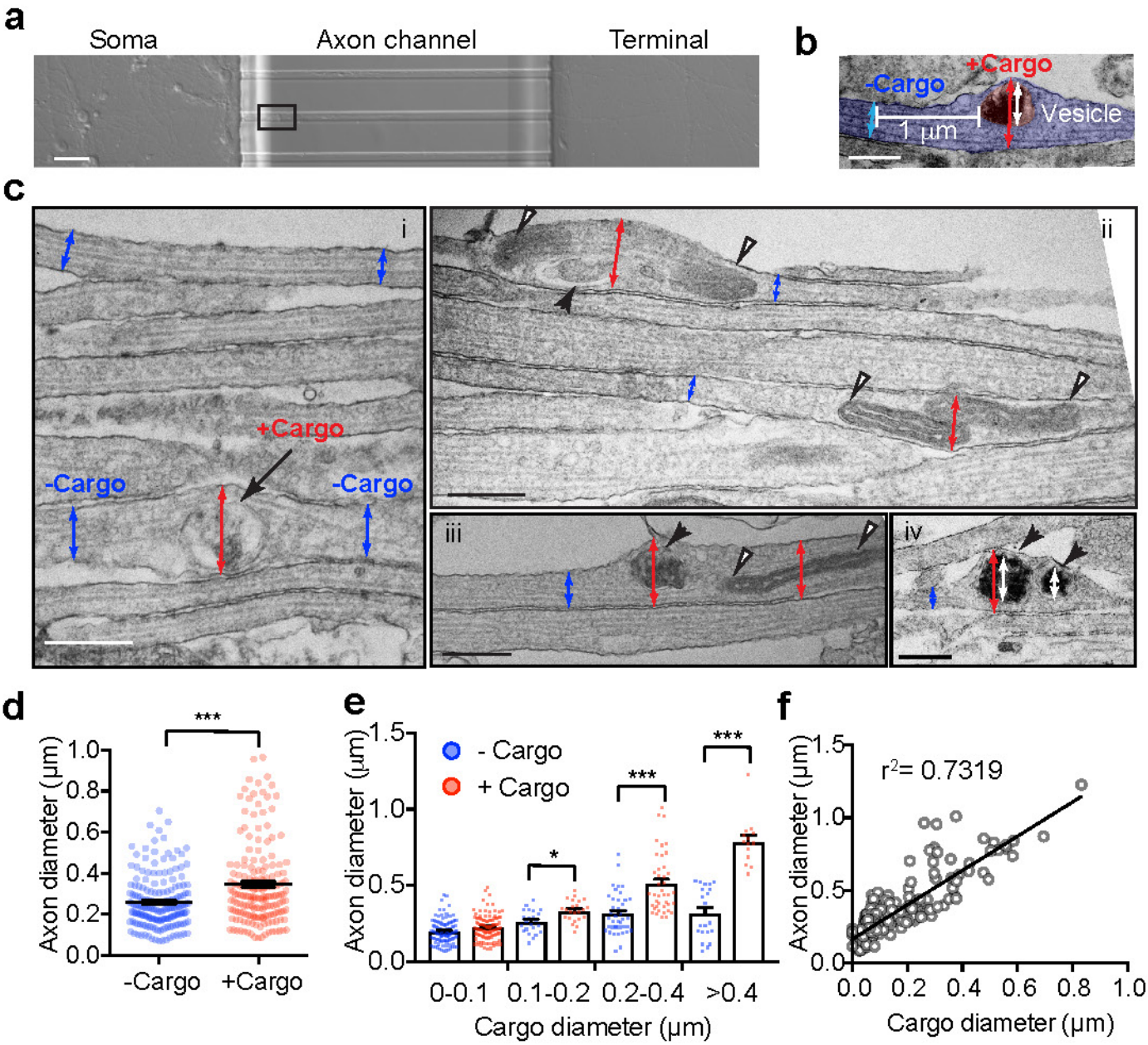

Figure 2. The size of axonal cargoes correlates with the transient radial expansion of axon shafts.

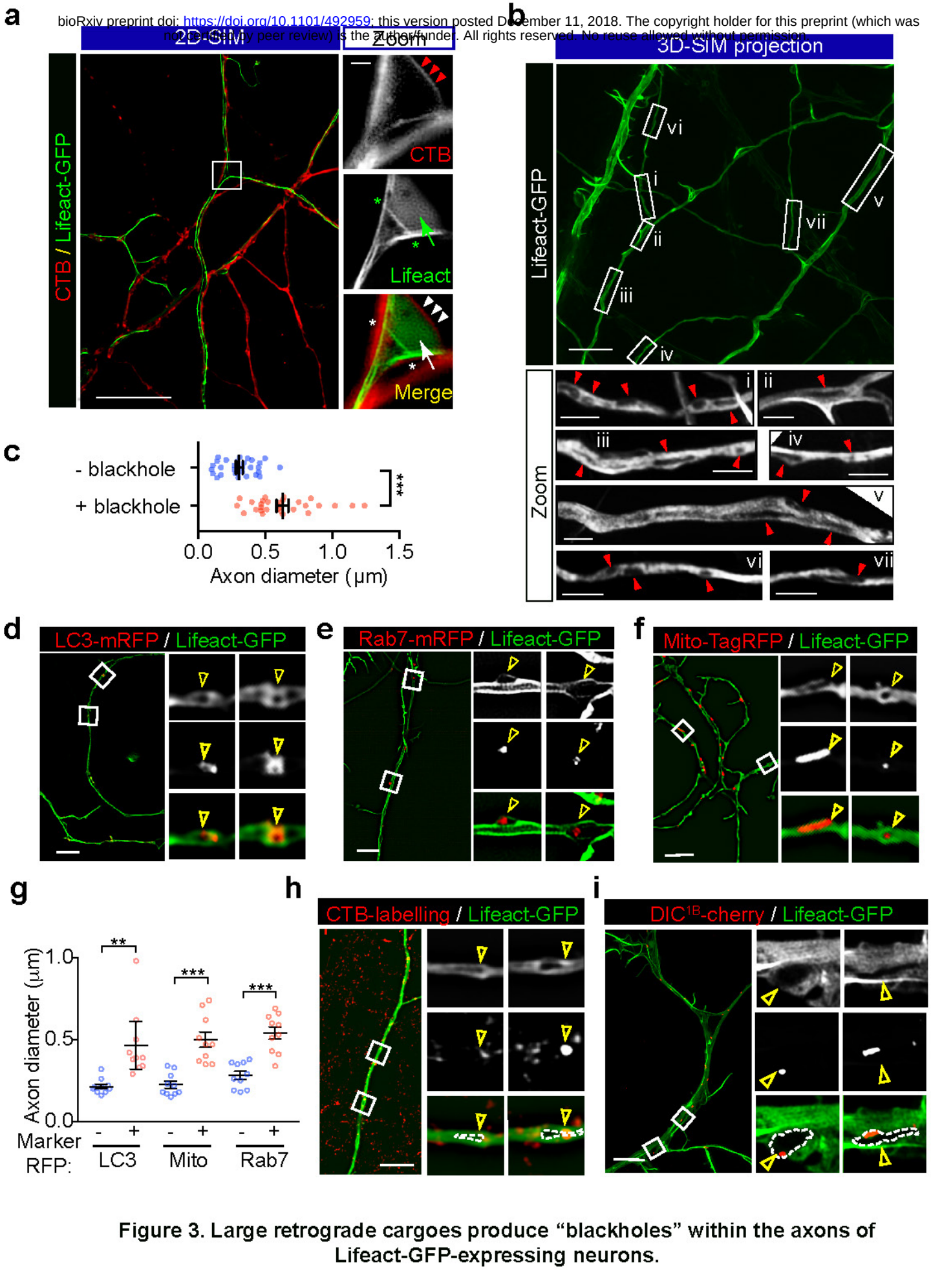

Figure 3. Large retrograde cargoes produce "blackholes" within the axons of Lifeact-GFP-expressing neurons.

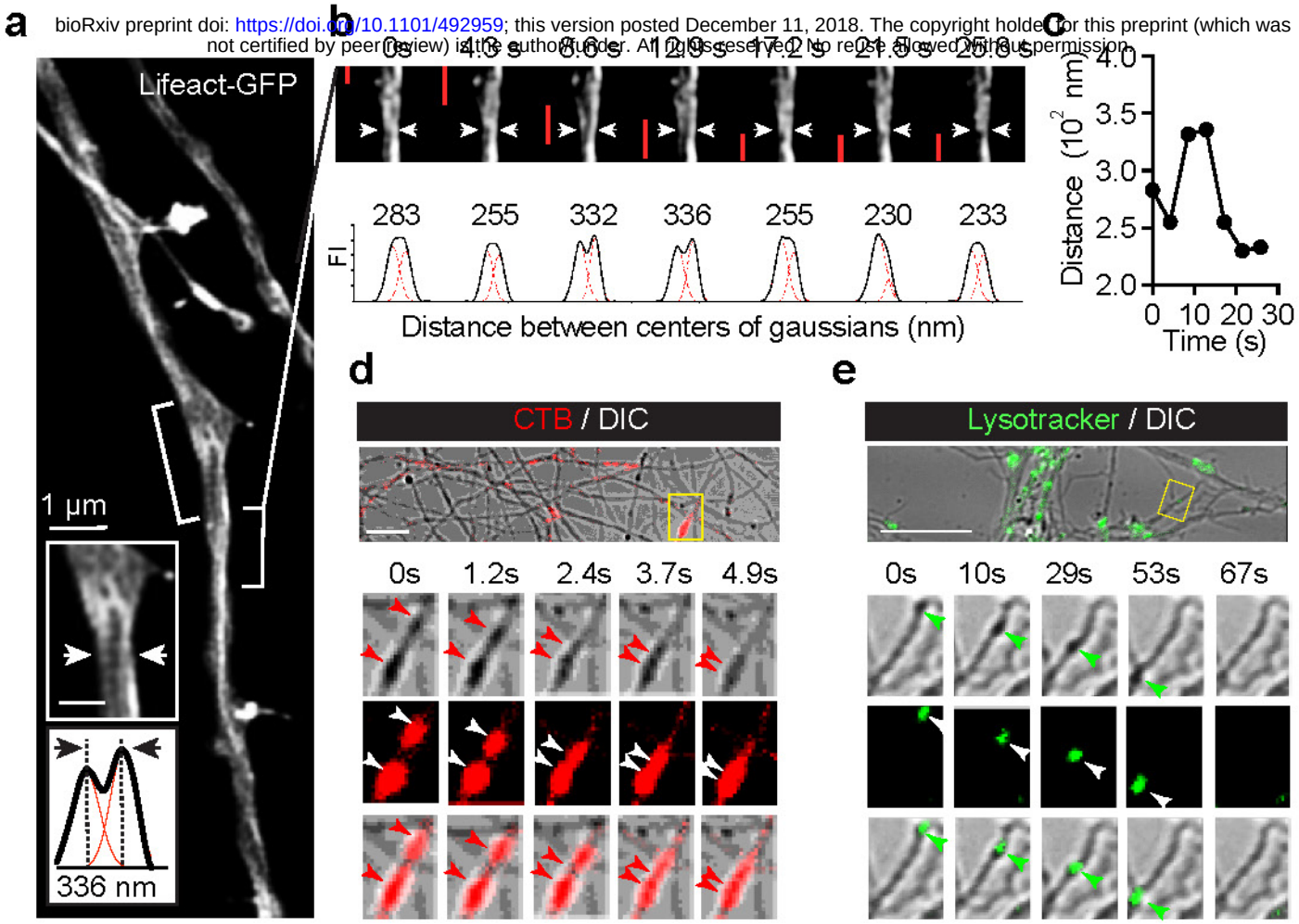

Figure 4. The transit of cargo causes a transient radial expansion of the axon.

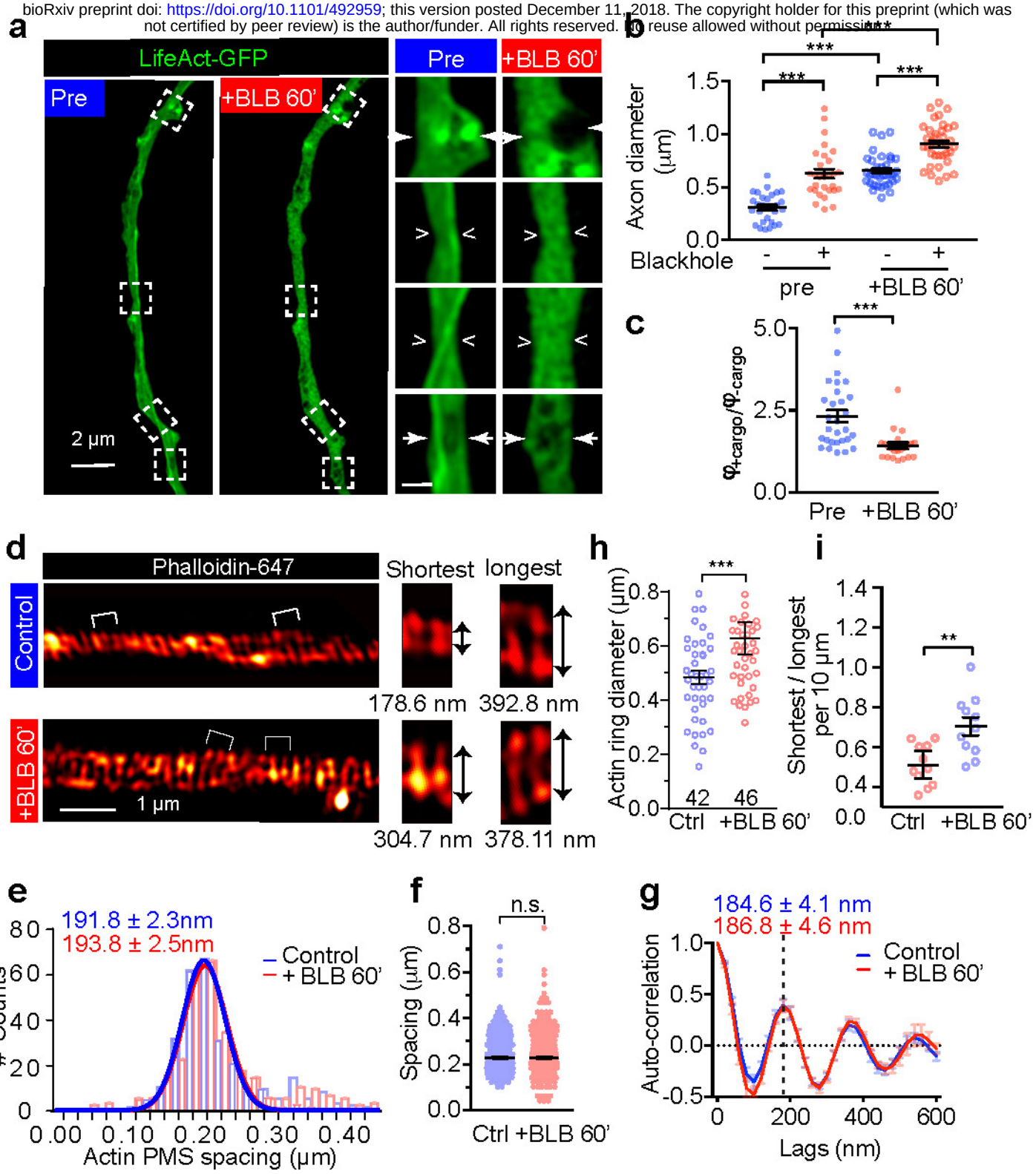

Figurer 5 Short-term inactivation of NM-II increases the axon diameter without affecting the actin ring periodicity.

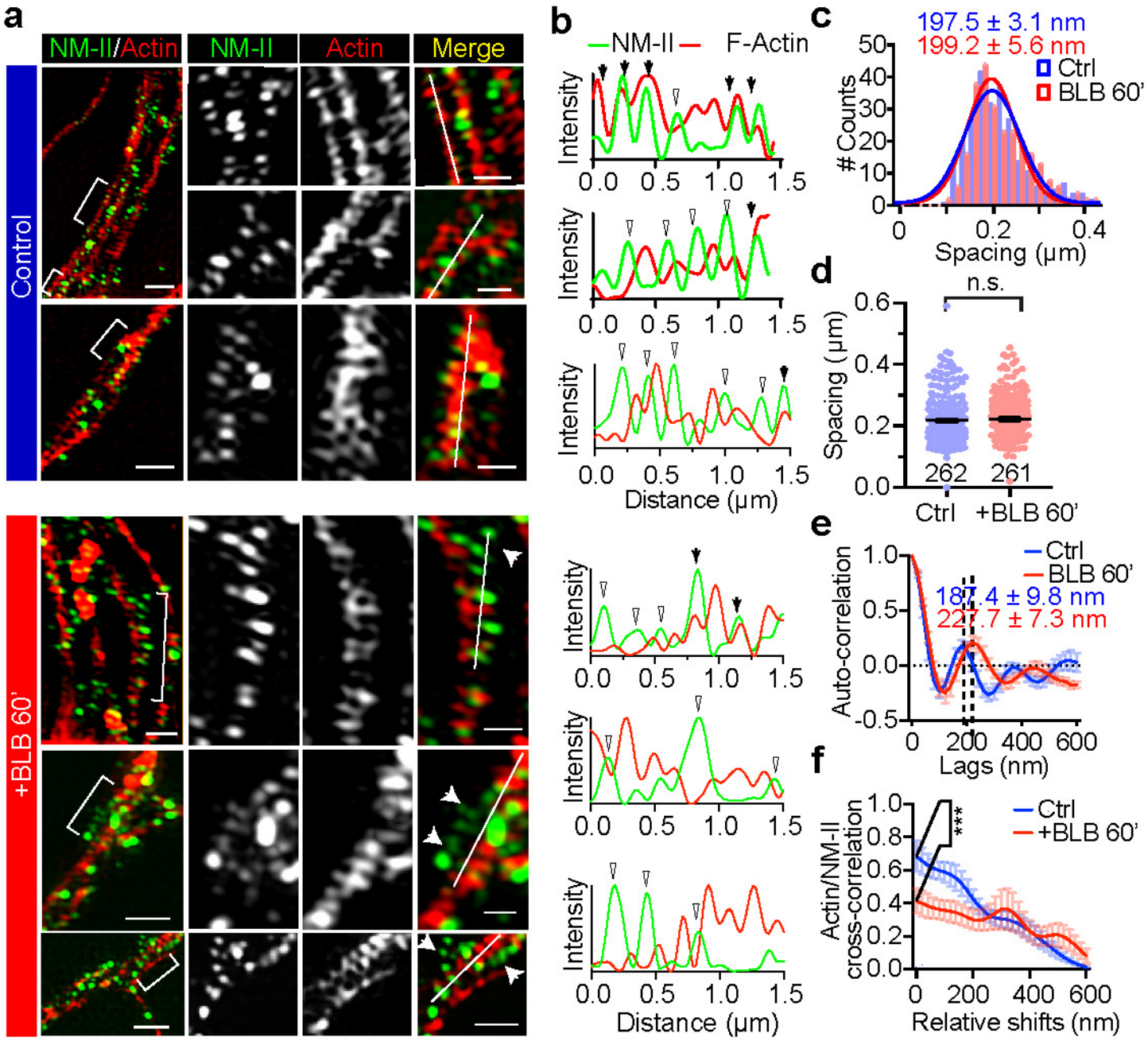

Figure 6. NM-II immunostaining reveals a periodic pattern that correlates with the periodic actin rings along the axons.

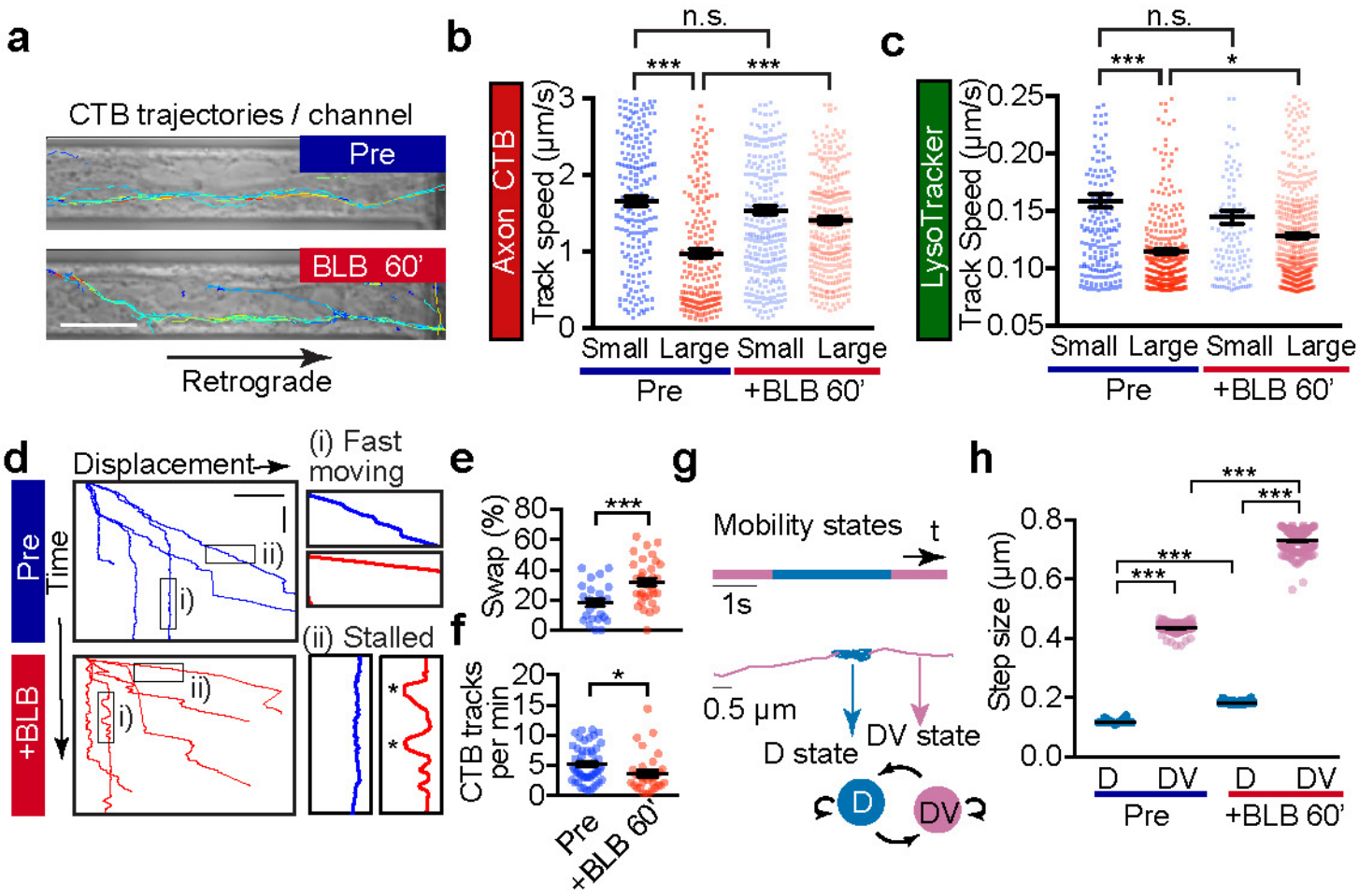

Figure 7. Short-term inactivation of actomyosin-II reduces the retrograde transport efficiency.

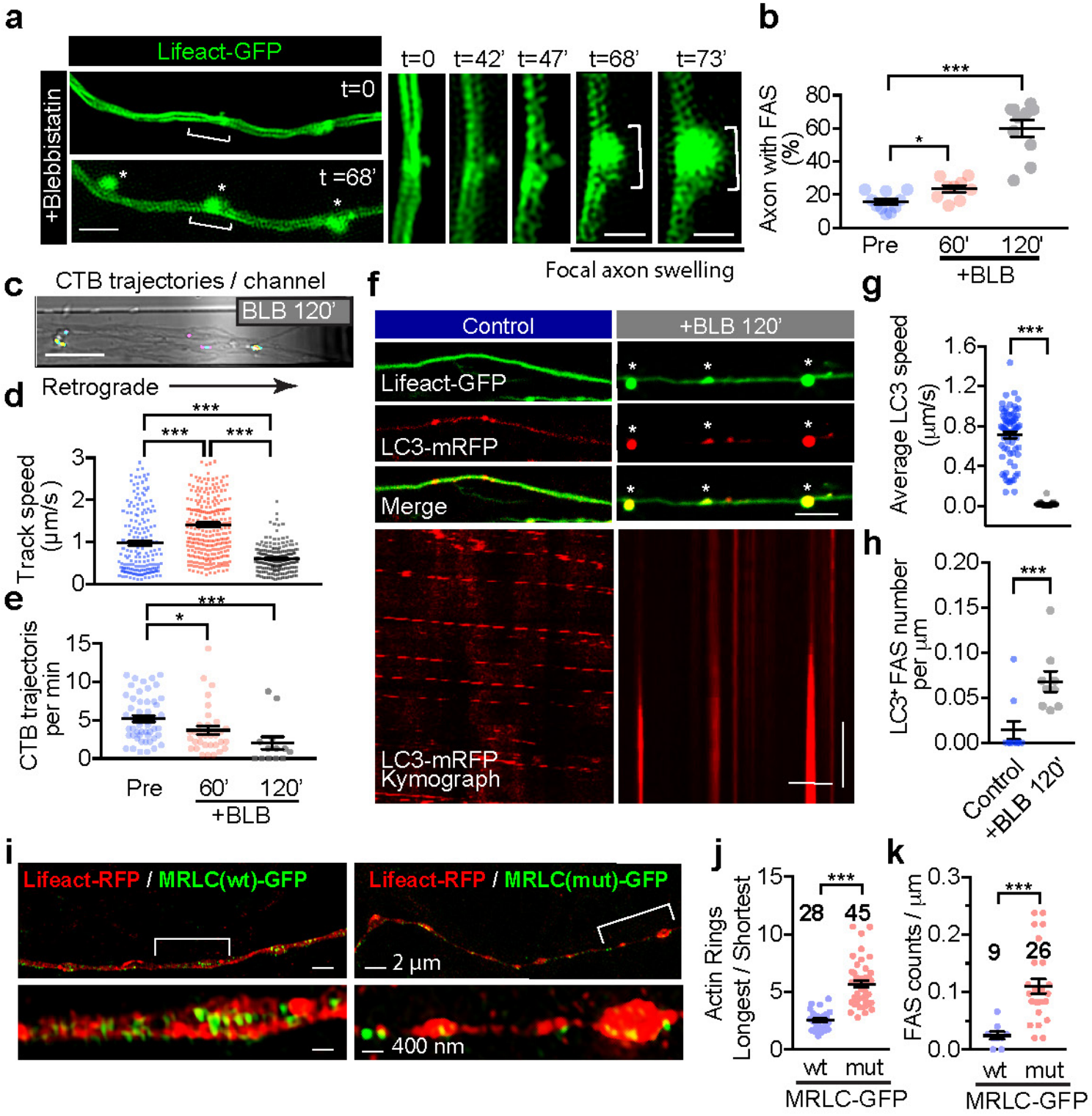

Figure 8. Long-term inhibition of actomyosin-II activity triggers accumulation of stalled cargo in focal axonal swellings (FAS).